Rijksuniversiteit Groningen

Bachelor Thesis

Revisiting the Radio Dichotomy of Quasars

by Separating Star Formation and AGN

Author:
C. M. Wortelboer

Supervisor:
Dr. L. Wang

Contents

Abstract

This thesis revisits the debate about the radio-loudness dichotomy by separating the total luminosity in the radio and optical bands into two components: star formation (SF) and active galactic nuclei (AGN). Afterward, the obtained distribution is examined as a function of quasar properties. The parameter used for the radio-loudness is given as $\mathcal{R} = L_{144\ \mathrm{MHz}}/L_i$. I used the SDSS DR16 Quasar catalog and cross-matched it to radio data from LOFAR, far-infrared data from Herschel, ancillary x-ray data from eROSITA and Chandra, and mid-infrared data from WISE. With the cross-matched data, SEDs were modeled by a multi-wavelength SED fitting code: CIGALE. The SEDs provided AGN fractions to separate the SF in the i-band. The LOFAR 144 MHz luminosity was separated by converting the total infrared dust luminosity, obtained by CIGALE, into 144 MHz radio luminosity. This was done using the far-infrared radio correlation (FIRC). The result was subtracted from the total. The separated distribution of $\mathcal{R}$ shows a slight bump which might hint at a potential dichotomy. However, no obvious bimodality was found. Quasar properties portray weak to no dependencies on $\mathcal{R}$. Although weak, the different correlations could indicate that radio-loudness is a quasar property that changes with the evolution of quasars.

1 Introduction

1.1 The radio dichotomy of Active Galactic Nuclei

Active galactic Nuclei (AGN) are known to produce non-stellar emissions expanding over multiple wavebands of the electromagnetic spectrum. Their radiation has been observed to consist of radio, microwave, infrared, optical, ultra-violet, x-ray, and gamma-ray waves (Padovani et al. (2017)). AGN blast out jets that are a result of mass accretion onto the supermassive black hole (SMBH) situated at their centers (e.g. Kormendy and Richstone (1995), Magorrian et al. (1998), Ferrarese and Merritt (2000)). In this paper, radio emission of quasars (type of AGN) is taken as the main focus of the research. Traditionally, quasars have been divided into two categories: radio-loud (RL) and radio-quiet (RQ) (e.g. Kellermann (1964), Strittmatter et al. (1980), Stocke et al. (1992)). In order to determine these categories the radio-loudness parameter is used. Mostly this parameter is defined as the logarithmic ratio of the radio to the optical luminosity or flux density (e.g. Kellermann et al. (1989), Stocke et al. (1992), Ivezić, Ž. et al. (2002), White et al. (2007), Baloković et al. (2012), Gürkan et al. (2019)). The bands in which this parameter is measured vary per study. As an example, the radio-loudness distribution found by Kellermann et al. (2016) is shown in Figure 1. The radio luminosity was measured at 6 GHz and the optical luminosity at the frequency of the SDSS i-band. (see Section 2.1). Kellermann et al. (2016) claimed to have found a radio dichotomy, as about 20% of his sample was found to have $L_{6\ \mathrm{GHz}} \gtrsim 10^{23}$ W Hz^{-1}.

Around ∼10% of cataloged quasars are identified to be radio-loud (Goldschmidt et al. (1999), Gaur et al. (2019)). The other ∼90% of (radio-quiet) quasars are also able to produce radio emission, but not as powerful as radio galaxies and the RL quasars (Doi et al. (2013), Condon (1992a)). The Radio-loudness of a quasar is a quantity mostly The physical processes that drive RL jets (and some RQ jets) remain uncertain. A theoretical model by Blandford and Znajek (1997) proposes that the production of these jets is created by the central spinning black hole, threaded by magnetic field lines. On the other hand, it is proposed that the jets are caused by AGN feedback when the accretion disk of the AGN is positioned in a particular manner concerning the orientation of the magnetic field from the SMBH (Blandford and Payne (1982)). However, there is no observational evidence to prove these theories and it can therefore not be concluded with certainty that the spin and the magnetic field of a BH has a causal connection to radio jets. Many researchers have found strong dependencies of radio-loudness on the SMBH

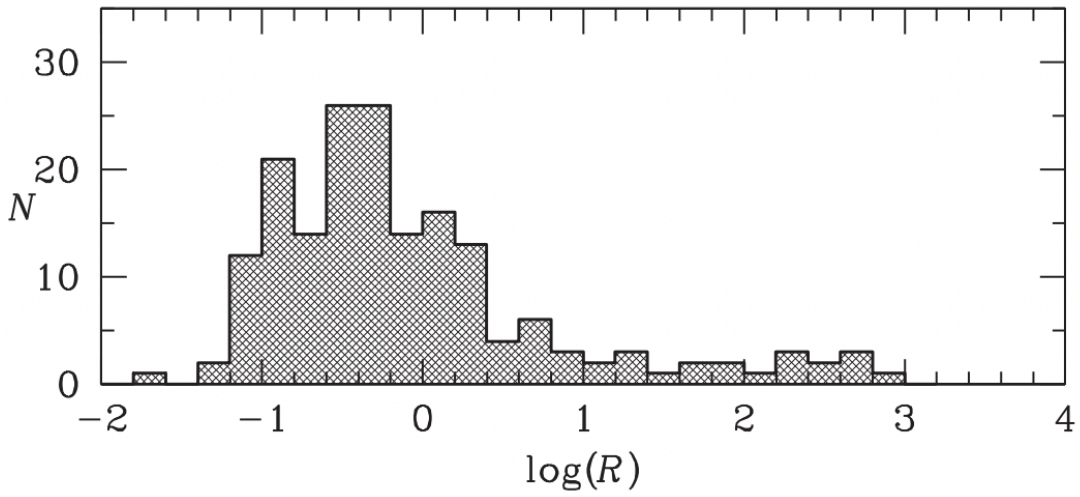

Figure 1: The radio-loudness distribution as found by Kellermann et al. (2016). $\log_{10}(L_{6\ \mathrm{GHz}}/L_i)$ is defined as the radio-loudness parameter. With this result, Kellermann et al. (2016) claimed to have found a radio dichotomy. The paper found the RL quasars to have $L_{6\ \mathrm{GHz}} \gtrsim 10^{23}$ W Hz^{-1} (Kellermann et al. (2016)).

mass (e.g. Lacy et al. (2001), Dunlop et al. (2003), Best et al. (2005)). This finding is also supported by observations showing that RL quasars tend to cluster together more strongly than RQ quasars, due to their larger SMBH mass (Retana-Montenegro and Röttgering (2017)). On the contrary to jets, it has been suggested that star formation (SF) is the dominant source of the radio emission from RQ quasars, proposing that the AGN in these host galaxies either have incredibly weak radio jets or produce no jets at all (e.g. Radcliffe (2021), Kellermann et al. (2016)). However, this conclusion has been rebuked, implying that the radio emission from SF is not enough to explain the radio emission, as the radio emission from SF is much smaller than the observed value (e.g. Zakamska et al. (2016)). What the eventual physical process is that dominates radio emission from RQ quasars, therefore, remains uncertain. SF and radio jets are not the only radio sources from AGN that can contribute to radio emissions. Other possible mechanisms contributing to the total AGN radio emission could be accretion disc winds, coronal disk emission, and low-power jets (Panessa et al. (2019)). In this project, the debated bimodality of RL and RQ quasars will be investigated. Determining this distinction between quasars proves relevant for the following reasons. First of all, further research into this quasar classification can be helpful to determine the different physical processes that release radio emissions. As mentioned before, these physical processes, in particular for RQ quasars, are currently not fully understood. The investigation of the quasar dichotomy can clarify these physical processes, like the properties and formation of relativistic jets from the AGN. Secondly, the differing radio-loudness between quasars could be an indicator of a quasar being in a specific evolutionary state. Some studies suggest that radio-loud quasars evolve into radio-quiet quasars over time (Garofalo and Bishop (2020), Garofalo et al. (2020)). Thus, by the dichotomy, the evolutionary track of quasars, their lifetimes and the conditions that regulate their radio jet activity could potentially be inferred.

1.2 Observational evidence

Whether the dichotomy between RL and RQ quasars is a clear-cut separation, is not yet certain. Some studies advocate the separation (e.g. Kellermann (1964), Ivezić, Ž. et al. (2002)) whereas results of others contradict it (e.g. Cirasuolo et al. (2003), Gürkan et al. (2019), Macfarlane et al. (2021)). In addition, others remain undecided (Baloković et al. (2012)). There are various reasons for disagreement in this area since classification methods vary. A quasar can be classified as RQ to one, but RL to the other. Furthermore, the radio-loudness of a quasar is by most studies defined to be the ratio between the radio and the optical flux density or luminosity (e.g. Kellermann et al. (1989), Ivezić, Ž. et al. (2002), White et al. (2007), Baloković et al. (2012), Gürkan et al. (2019)). These observed properties can be affected by the use of different radio and optical bands, causing inconsistent results (e.g. Kellermann et al. (1989), Ivezić, Ž. et al. (2002), Jiang et al. (2007)).

Aside from testing the existence of the AGN radio-loudness dichotomy, the parameter has moreover been investigated as a function of other quasar properties. These properties include redshift, bolometric luminosity, and nuclear properties: Black hole mass and Eddington ratio λ_{Edd}. For instance, Jiang et al. (2007) presented a strong correlation between radio-loudness and both redshift and optical luminosity. As for black hole mass, Laor (2000) found a correlation between AGN radio-loudness and black hole mass. This correlation unfolds further in determining an upper limit in black hole mass for practically all RQ quasars of 3×10^8 $M_\odot$, and RL quasars portraying a lower black hole mass limit of 3×10^9 $M_\odot$. Confirming this separation of black hole mass for the two types of quasars, Metcalf and Magliocchetti (2006) concluded to have found the result that RL AGN have a larger black hole mass on average, whereas RQ AGN on average have lower black hole masses. On the contrary, not every study has found a radio-loudness to black hole mass correlation. For example, no correlated relationship was found by Ho (2002), contradicting Laor (2000) by stating that RL quasars in his sample are not solely restricted to high black hole masses but can exhibit masses as low as 10^6 $M_\odot$. This comparison is shown in Figure 2. The figure from Laor (2000) clearly shows that quasars with a large radio-loudness have larger black hole masses. The black hole relationship from Ho (2002) on the other hand shows a more scattered relationship. No clear distinction as found by Laor (2000) is obtained. Differences in these results can be a cause of a different radio-loudness parameter. Laor (2000) used a radio-loudness ratio given by: $R = f_\nu(5\text{ GHz})/f_\nu(4400\text{A})$. Ho (2002) on the other hand, defined the parameter as: $R' = L_\nu(6\text{ cm})/L'_\nu(\text{B})$. Where $L'_\nu(\text{B})$ is the B-band luminosity calculated from x-ray luminosity measured in the hard x-ray (2-10 keV) band.

Aside from finding a relationship between the radio-loudness and black hole mass, it has been investigated whether radio-loudness is correlated with λ_{Edd}. Most studies find an anti-correlation (e.g. Ho (2002), Nagar et al. (2005), Sikora et al. (2007)).

1.3 Difference in methods with respect to previous studies

This thesis revisits the calculation of the radio quasar dichotomy separating radio-quiet and radio-loud quasars. The methods used to determine whether this bimodality exists or not differ from findings of, for example, Cirasuolo et al. (2003) and Gürkan et al. (2019). In these studies, the radio-loudness parameter was determined by using the total radio luminosity of the quasars. This method does not take into account the component of the radio luminosity that is caused by SF. Not accounting for this contribution can lead to inaccurate results in determining the existence of a potential quasar dichotomy. The goal of this project is to separate the SF contribution so as to obtain a radio-loudness distribution that is not influenced by this factor. This method could potentially lead to a radio-loudness distribution that might be different from previous results,

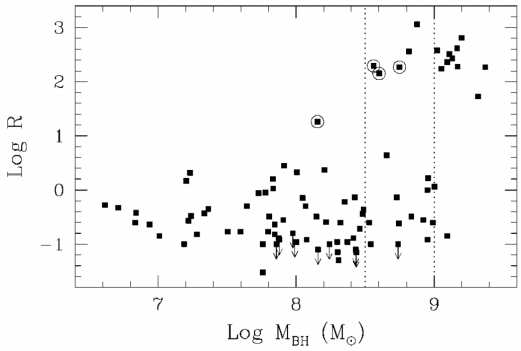

(a) Radio-loudness as a function of black hole mass (Laor (2000)).

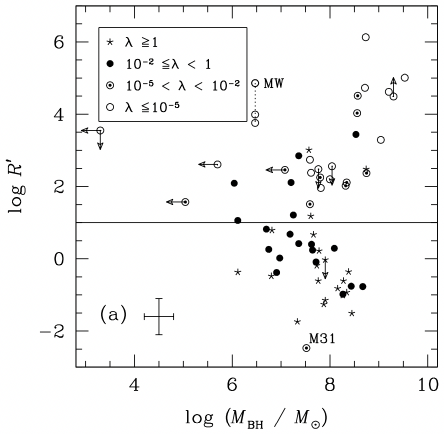

(b) Radio-loudness as a function of black hole mass (Ho (2002)).

Figure 2: Two plots from different studies showing the relationship between the radio-loudness and black hole mass. Figure 2a shows that RL quasars have higher black hole masses, whereas in Figure 2b this relationship is not of the order.

like the one shown in Figure 1. SF has been accounted for in a previous study, and showed a result similar to Figure 1 (Macfarlane et al. (2021)). The results obtained by Macfarlane et al. (2021) show that RL quasars are not distinctly separated from RQ quasars. They are however the luminous continuation of the AGN jet emission distribution. Although my study is fundamentally similar to Macfarlane et al. (2021), assuming a superposition of the AGN jet emission and SF luminosity, the methods employed to conclude the potential existence of the quasar dichotomy in this thesis differ. In Macfarlane et al. (2021), the radio emission from both AGN and SF is modeled to fit observational radio data, and the best-fit parameters from these models are taken to expand on the analysis. In this project, however, the contribution of the star formation and AGN luminosity is calculated from observed data directly. However, spectral energy distributions (SEDs) are modeled which are used to separate the SF component from the data. The modeling of the SEDs will be done with CIGALE, a multi-wavelength SED fitting code (Boquien et al. (2019)) with an improved fitting mechanism by Yang et al. (2022). From these SEDs, the AGN emission fraction in the i-band can be determined and can thus be incorporated in determining the radio-loudness parameter. As for removing the SF component in the radio luminosity, the far-infrared radio correlation (FIRC) will be utilized. The FIRC is an empirical correlation relating the far-infrared luminosity and the radio luminosity emitted by galaxies (e.g. van der Kruit (2005), de Jong et al. (1985), Yun et al. (2001)). The correlation suggests a relationship between SF and the presence of magnetic fields in galaxies. Apart from radio emission by AGN, the radio emission from star-forming quasars is a product of synchrotron radiation from cosmic rays, hypothesized to be accelerated in supernova remnants. Supernovae mostly occur in star-forming regions of the galaxy, meaning star formation is directly related to radio emission, excluding AGN emission Condon (1992b). This means that the FIRC can be used to convert infrared luminosity into radio luminosity by correlation. An example of this correlation is shown in Figure 3 (McCheyne et al. (2022)). Simply put, the plot shows a linear correlation between the total infrared luminosity (8-1000 µm) as a function of the radio luminosity at 150 MHz. Compared to Macfarlane et al. (2021), this method of separating SF contribution from the total luminosity allows for a more accurate calculation. This is because it takes into account

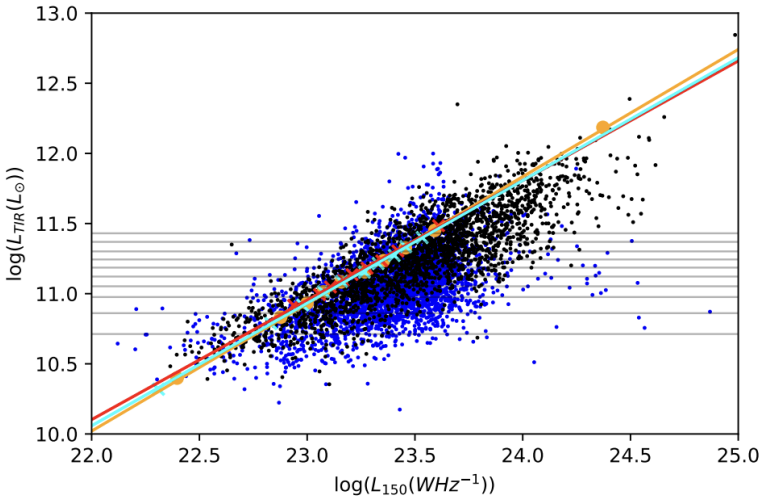

Figure 3: The FIRC with the logarithmic total infrared luminosity ($L_{\nu,\mathrm{TIR}}$) as a function of the logarithmic radio luminosity at a frequency of 150 MHz ($L_{\nu,150\ \mathrm{MHz}}$). The line in orange represents the linear fit to the data (McCheyne et al. (2022)).

empirical data for each quasar within the sample. A more detailed description of the methods is given in section 3.

With each study claiming different answers and using varying methods, it is hard to verify whether a radio dichotomy truly exists or not. Therefore, this thesis will use the same radio-loudness parameter as Gürkan et al. (2019) and compare its radio-loudness distribution to the one found here. The radio-loudness distribution found in Gürkan et al. (2019) is shown in Figure 4. Just as Figure 1 the distribution seems to have no dichotomy. The difference between these studies however, is that Kellermann et al. (2016) concludes to have found a separation between RQ and RL quasars, whereas Gürkan et al. (2019) rejects this claim. The radio-loudness parameter is defined as $\mathcal{R} = \log_{10}(L_{144}/L_i)$. Where L_{144} is the radio luminosity at a frequency of 144 MHz and L_i the luminosity of the i-color filter from the SDSS (see section 2.1) at a wavelength of 7625 Å. The final units of each luminosity are in W Hz^{-1}. In Gürkan et al. (2019) the radio-loudness parameter was calculated for a sample of 30,897 quasars observed in the HETDEX spring (Hill et al. (2008)) and the LOFAR H-ATLAS/NGP field (Hardcastle et al. (2016)). No radio-loudness dichotomy was found and the paper concluded that radio-loudness is a continuum of quasar radio properties, rather than being a distinct property of two extremes. Concerning the relationships between the radio-loudness and other quasar properties, the results of the paper make clear to have found no strong correlations between the radio-loudness and both the black hole mass and λ_{Edd}. By taking the same radio-loudness parameter, yet conducting the research differently, it can be determined whether removing the component of SF from the total radio and optical luminosity has a significant impact on these correlations. If the results established in this thesis are fundamentally different from those in Gürkan et al. (2019), the SF component contributing to the total luminosity can be concluded to significantly affect the radio-loudness distribution.

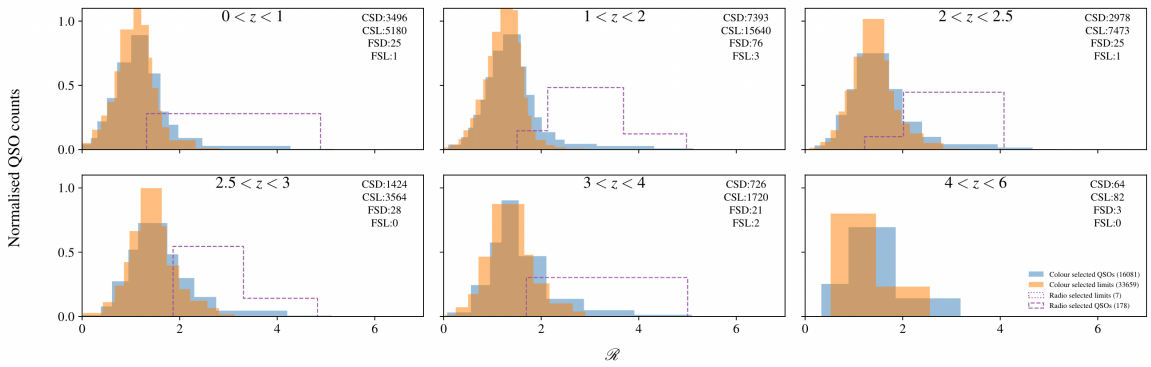

Figure 4: The radio-loudness distribution divided over six redshift bins. The colors of the histogram represent different source selections (Gürkan et al. (2019)). The overall shape of the distributions is very similar to the radio-loudness distribution in Figure 1, found by Kellermann et al. (2016).

1.4 Outline of the thesis

The structure of this paper is as follows. In Section 2, the quasar sample will be described, including the various datasets supplying information about the quasar fluxes in different wavebands. Methods taken to obtain the quasar sample are listed here as well. Section 3 contains the methods taken for the various results. First, a method will be described to obtain a clear distinction to determine the existence of a quasar dichotomy. Secondly, the procedure of the SED analyses by CIGALE will be presented along with the methods of using these models to determine the intrinsic star formation luminosity component in the i-band and eventually, the luminosity emitted by AGN alone. Utilizing the FIRC to obtain the same luminosity separation will be described here as well. Section 4 presents the eventual results. These results include the radio-loudness quasar distribution before and after separating the SF and AGN luminosity components. Furthermore, the relationship between radio-loudness and other quasar properties like redshift, bolometric luminosity, black hole mass, and λ_{Edd} will be presented. Section 5 discusses these findings and judges their relevance and accuracy. At last, the report is finalized with a conclusion in section 6.

2 Data

My quasar sample is taken from the Sloan Digital Sky Survey (SDSS) DR16 quasar catalog. This dataset is the final catalog of the SDSS-IV quasar program/the extended Baryon Oscillation Spectroscopic Survey (eBOSS; Dawson et al. (2016)). Therefore, this catalog contains the most up-to-date quasar ids and redshifts. The goal of the data selection in this thesis is to cross-match various datasets to the quasar catalog. As a result, I am left over with a dataset that contains quasar ids, redshifts, and observational data in various bands. This information is necessary for CIGALE to model proper SEDs (see Section 3.2). In this study, the optical data is obtained through SDSS, radio data through LOFAR, the infrared data through both the WISE and Herschel telescope, and finally, the x-ray data is taken from the XMM-Newton telescope, eROSITA, and Chandra. The bands of each data survey are described below. The fields analyzed are the H-ATLAS/NGP field, the GAMA09 field, the XMM-LSS field, and the LOFAR deep fields: Boötes, Lockman, and ELAIS-N1. All quasars selected from each field are combined for

a maximized quasar sample. The fields are visualized in Figure 5.

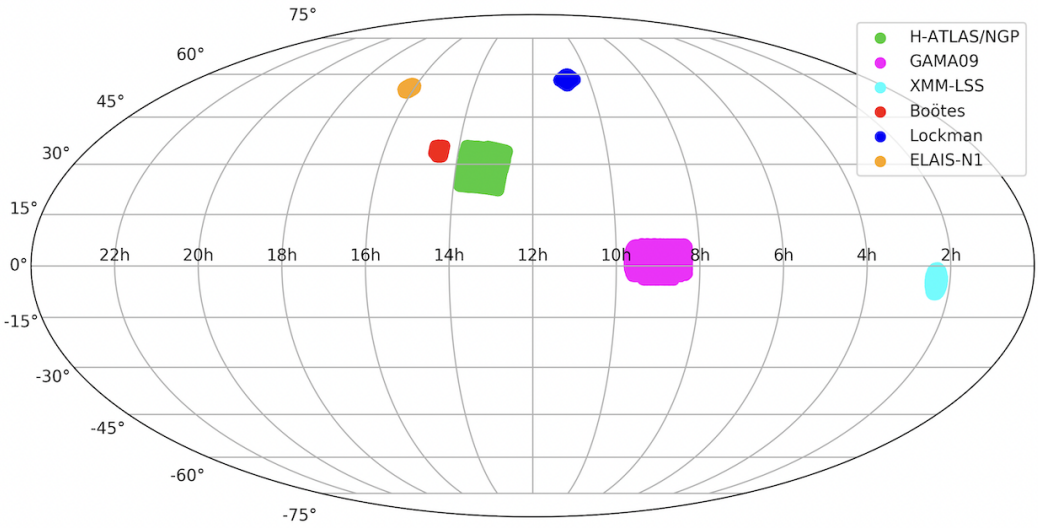

Figure 5: Visualization of the different fields used for data extraction. Their R.A. and decl. are mapped onto a Mollweide projection of the sky. The plot uses the equatorial coordinate system.

2.1 The Sloan Digital Sky Survey (SDSS)

The finalized quasar sample is a selected set of quasars taken from the SDSS quasar catalog 16th data release (Lyke et al. (2020)). The quasars are all identified by spectroscopy and selection algorithms along with the means of visual inspection. A description of the target process is given by Myers et al. (2015). Estimated values for the "primary" redshifts are for the most part visually inspected. Visually inspected redshifts from, for example, the SDSS DRQ7 and DRQ12 catalogs are included. If no visually inspected redshift was available, a redshift was determined by the SDSS automated pipeline redshift (Lyke et al. (2020)). The quasar catalog contains 750,414 quasars and spans 7500 $\deg^2$ of sky area. The sky coverage is given in Figure 6. For the cross-matching process in every observation field, the value-added DR16 quasar catalog is utilized. This catalog contains data from each of the four observation projects: SDSS-I, II, III, and IV. Data contained within this dataset are i-band absolute magnitudes and multi-wavelength cross-matched data from other observation sources. The set contains data from the telescopes: GALEX, UKIDSS, WISE (W1 and W2), FIRST, 2MASS, 2RXS, XMM-Newton, and Gaia. For the final dataset, the following bands were used: u (0.3543 µm), g (0.4770 µm), r (0.6231 µm), i (0.7625 µm), and z (0.9134 µm). These are optical color filters of the SDSS itself. For these bands, the 5σ detection limit in AB magnitudes is 22.0, 22.2, 22.2, 21.3, and, 20.5 (Ivezić, Ž. et al. (2002)). Two infrared bands from the DR16Q catalog were used as well, namely the two available WISE bands: WISE1 (3.368 µm) and WISE2 (4.168 µm). From XMM-Newton was taken the total flux, meaning the soft and hard x-ray flux bands combined, yielding a total band with an energy range of 0.2 - 12 keV.

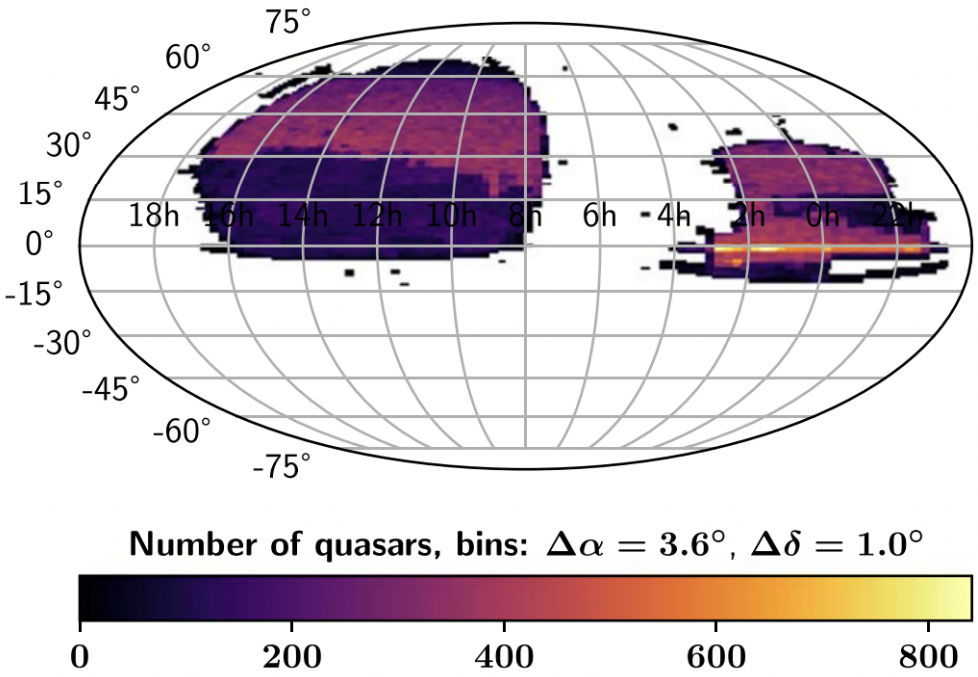

Figure 6: Visualization of the SDSS DR16 quasar catalog sky coverage. R.A. and decl. are mapped onto a Mollweide projection of the sky. The plot uses the equatorial coordinate system (Lyke et al. (2020)).

2.2 The LOw-Frequency ARray (LOFAR)

The obtained radio catalogs are all taken from LOFAR. For the H-ATLAS/NGP field in particular, the dataset used is LoTSS DR2, a radio survey of two regions covering the northern sky. Each region has a sky coverage of 4178 deg^2 and 1457 deg^2 respectively. The dataset contains a total of 4,396,228 objects observed at an angular resolution of 6" and is described by Shimwell et al. (2022). The data from LOFAR provides extremely accurate source coordinates, having a sensitivity better than 100 µJy beam^{-1} (Mandal et al. (2021)). Data for the LOFAR deep fields are taken from the dataset LoTSS Deep Fields DR1, covering three fields: Bootes, Lockman Hole, and ELAIS-N1. The data for Bootes and Lockman Hole are described by Tasse et al. (2021). The central frequency of this data is currently taken at 144 MHz but was initially observed at a central frequency of 150 MHz as well. Data taken from the observation field ELAIS-N1 on the other hand is described by Sabater et al. (2021) and has a central frequency of 146 MHz. The collected radio data from these fields have been cross-matched with additional data having bands covering the UV to MIR, including FIR data from the Spitzer and Herschel telescopes (Kondapally et al. (2021)). These additions provide the fields with data taken in the PACS and SPIRE bands as described in section 2.3. As a result of crossmatching with data from Spitzer, the full dataset contains data taken from Multiband Imaging Photometer for Spitzer (MIPS, at 24 µm, Rieke et al. (2004)) and the Infrared Array Camera (IRAC, at 3.6, 4.5, 5.8 and 8.0 µm, Fazio et al. (2004)) as well. These bands are not included in the data analysis of this thesis. The reason for this is to reduce the load of data processing (see 3.2). The sky coverage of the cross-matched fields is 9.5 deg^2 (Boötes), 10.73 deg^2 (Lockman Hole), and 7.15 deg^2 (ELAIS-N1). For the remaining fields XMM-LSS and GAMA09, separate LOFAR fields were utilized with a central frequency of 144 MHz. LOFAR data taken from the GAMA09 field is not to be

distributed. Specifications about the radio data taken in the XMM-LSS field are described by Hale et al. (2019). These radio observations in the XMM-LSS encompass 27 deg^2 of the field.

2.3 The Herschel Multi-Tiered Extragalactic Survey (HerMes)

Further infrared data were taken from three different instruments part of the Herschel telescope: The Spectral and Photometric Imaging Receiver (SPIRE, Griffin et al. (2010)) and the Photodetector Array Camera and Spectrometer (PACS, Poglitsch et al. (2010)). These datasets are part of the Herschel Extragalactic Legacy (HELP) project. In total, PACS and SPIRE contribute to data of 5 bands and all operate in the FIR wavelength range. From PACS these are the green (100 µm) and the red band (160 µm). PACS has an expected sensitivity of 3-4 mJy beam^{-1}. SPIRE contains three bands: PSW (250 µm), PMW (350 µm), and PLW (500 µm). The expected sensitivity is approximately 2-8 mJy beam^{-1}. The angular resolution of the Herschel telescope is given by 7"$\times(\lambda_{obs}/100\ \mu m)$ (Pilbratt et al. (2010)). Fluxes of the observed objects were measured using XID+, a Bayesian probabilistic de-blending tool, capable of extracting the source flux density of a galaxy from photometry maps suffering from source confusion (Hurley et al. (2017)). For all fields most of this data was available. Only the XMM-LSS and the GAMA09 fields lacked data in both the PACS green and red bands.

2.4 Ancillary data

2.4.1 The Wide Field Infrared Survey Explorer (WISE)

Additional to the infrared data contained in HerMes, infrared data from the ALLWISE source catalog is utilized. This data is obtained from the WISE telescope, a telescope operating in the mid-infrared Wright et al. (2010). From the value-added SDSS DR16 quasar catalog, the WISE1 and WISE2 bands from this telescope are already available. In total, the telescope observes four bands. The final bands remaining are the WISE3 (12.082 µm) and WISE4 (22.194 µm) bands. The angular resolution of the four bands are 6.1", 6.4", 6.5", and 12", going in order from one to four. All reported magnitudes of the ALLWISE source catalog are in the Vega system and can be converted into Jansky by the following formula:

$$F_\nu(\text{Jy}) = F_{\nu_0} \times 10^{-m_{vega}/2.5} \tag{1}$$

Here F_ν(Jy) represents the source flux density in Jansky in a specific band, F_{ν_0} is the flux density in Janskys at a Vega magnitude of zero, as this formula is calibrated to the flux density of Alpha Lyrae (Vega). F_{ν_0} differs per band: 309.540 Jy (WISE1), 171.787 Jy (WISE2), 31.674 Jy (WISE3) and 8.363 Jy (WISE4). The formula also allows for a color correction but is ignored for the purposes of this thesis. The processing and archiving of the WISE data are realized by the Infrared and Analysis Center (IPAC), the NASA science center at the California Institute of Technology (Caltech). Software used for incoming data processing is based on algorithms and pipelines from the Two Micron All Sky Survey (2MASS), the Spitzer Telescope, and the Galaxy Evolution Explorer (GALEX) (Wright et al. (2010)).

2.4.2 Chandra

For the LOFAR deep field Boötes, a catalog with x-ray observations from the Chandra telescope was added (Kenter et al. (2005)). This survey encompasses 9 deg^2 of the Boötes field and contains a total of 3293 observed objects. On board, the Chandra telescope is the High-Resolution Camera (HRC), containing two detectors designated for the imaging (HRC-I) and spectroscopy (HRC-S) of x-ray objects. The off-axis angular resolution of the telescope is about 10" when at 10

arc minutes off-axis. The on-axis resolution on the other hand is of higher quality than 0.5" (Murray et al. (2000)). Because of the powerful angular resolution, Chandra is very well able to distinguish between closely spaced objects. This fact allows for a small separation angle when cross-matching (see Section 2.5). The x-ray observations span the energy range of 0.5 keV to 7 keV. From this range, the catalog contained data for three individual ranges: 0.5 - 7 keV, 0.5 - 2 keV, and 2 - 7 keV. All three observation bands were included in the final data analysis.

2.4.3 Extended ROentgen Survey with an Imaging Telescope Array (eROSITA)

Besides Boötes, another x-ray catalog was cross-matched to the flux data of the GAMA09 field. This catalog contains 27,369 objects and is a product of the x-ray observations by eROSITA, an x-ray telescope aboard the Spectrum-Roentgen-Gamma (SRG) mission. This survey covers a 140 deg^2 sky area and overlaps with the GAMA09 field. The angular resolution of eROSITA is about 28" averaging over the field of view. The on-axis angular resolution is about 15". The typical flux limit is approximately $\sim 10^{-14}$ erg $cm^{-2}s^{-1}$ and $\sim 10^{-14}$ erg $cm^{-2}s^{-1}$ for the 0.5-2 keV and 2-10 keV energy band respectively (Predehl et al. (2021)).

2.5 Cross-matching

Every cross-match started with the SDSS DR16 quasar catalog matched to the LOFAR datasets. Each of these cross-matches was done within a separation of 2". Doubles were removed[1]. Because LOFAR is extraordinarily sensitive, the coordinates determined by LOFAR were used to do further cross-matching. After cross-matching with LOFAR, the far-infrared datasets from Herschel were cross-matched. For the LOFAR deep fields: Boötes, Lockman Hole, and ELAIS-N1 this cross-match was unnecessary, due to this data already being contained within their value-added catalogs. For the other fields, the cross-match with data from HerMes was taken within 5", three arcseconds larger than the separation between the SDSS and LOFAR sources. This was done to account for the larger angular resolution of the Herschel instruments. Afterward, a cross-match was performed with the ALLWISE Source Catalog to obtain data from the WISE3 and WISE4 bands. These cross-matches were performed at a separation of 3", again taking into account the angular resolution of the WISE bands. The final cross-match was performed with the x-ray catalogs provided by the Chandra and eROSITA telescopes, available to only the GAMA09 (eROSITA) and Boötes (Chandra) fields. These cross-matches had a separation of 2". The yielded amount of cross-matches did not become the total number of the final dataset. Rather than the quasars being cross-matched, the X-ray data were added to the cross-matched catalog, thus leaving some quasars without this addition. Fortunately, the gaps in the finalized catalog do not pose a problem to the data analysis, as CIGALE can operate with missing data points (see 3.2). An overview of the total cross-matches for every catalog in each field is given in Table 1.

Concatenating all cross-matched datasets from every field, a final catalog of 1212 quasars has been obtained. For further analysis, however, quasars with faulty i-band magnitude values (given by a 1 or a 2) as given by the SDSS DR16 quasar catalog have been removed. In total, these were 6 quasars and 1206 quasars were left. A further restriction was done on the redshift. All quasars with a redshift higher than a 3 have been removed. After the selection, a total of 1154 quasars remained, which is used as the final sample for the analysis. The restriction of the redshift range is required due to the redshift evolution of the FIRC (see section 3.3). An overview of the total quasar selection will be given in table 1. The distribution of the final

[1]Double matches are eliminated for every cross-match in every field.

		Cross-matched Surveys with Maximum Separation in Arcseconds			
		S - L 2"	S - L - H 5"	S - L - H - AW 3"	S - L - H - AW - C/eR 2"
		Number of Matches			
Fields	H-ATLAS/NGP	57480	316	306	-
	GAMA09	405	55	-	36
	XMM-LSS	72	16	15	-
	Boötes	216	Already in Dataset	202	117
	Lockman	377	Already in Dataset	352	-
	ELAIS-N1	302	Already in Dataset	281	-

Table 1: Cross-matched datasets: SDSS DR16 Quasar catalog (S), LOFAR (L), Herschel (H), ALLWISE (AW) and Chandra (C)/eROSITA (eR). For each match the yield is presented. The total matches amount to 1211

sample's absolute k-corrected i-band Magnitude as a function of redshift is given in Figure 7 and that of the k-corrected 144 MHz luminosity in Figure 8.

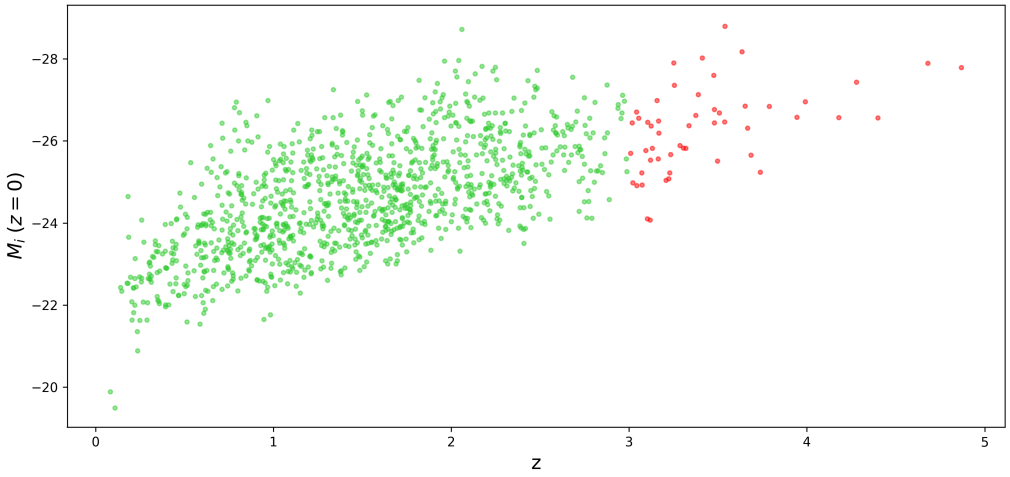

Figure 7: Visualization of the finalized quasar sample's absolute i-band magnitude given in green. The quasars with a redshift larger than three are displayed in red. These are not included in the final analysis.

3 Methods

3.1 The radio-loudness parameter

Having a quasar sample, the radio-loudness parameter can be determined. In this study, the radio-loudness parameter is defined to be the logarithmic ratio of the luminosity at 144 MHz, the central frequency of the LOFAR passband, to the i-band luminosity from which the absolute magnitude is obtained by the SDSS. Both luminosity parameters have units of W Hz^{-1}. The

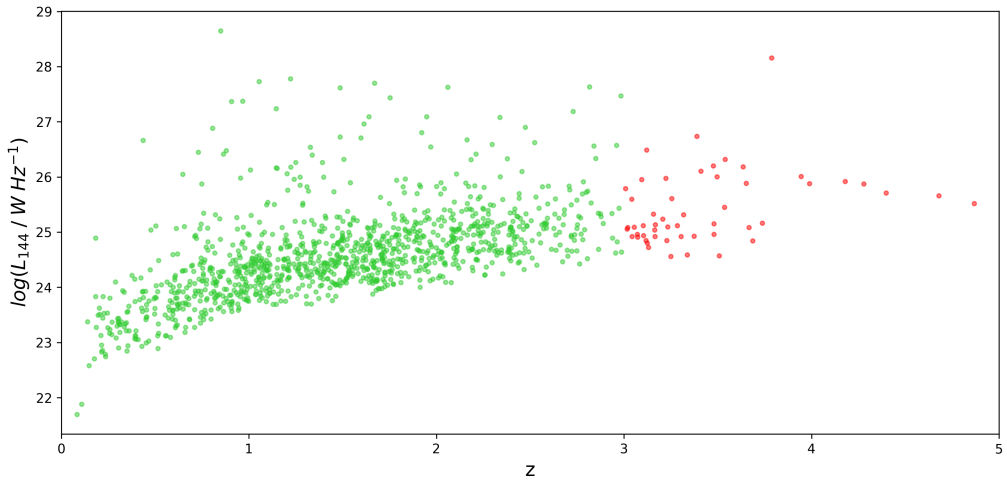

Figure 8: Visualization of the finalized quasar sample's luminosity at a central frequency of 144 MHz given in green. Units are in W Hz^{-1}. The quasars with a redshift larger than 3 are displayed in red. These are not included in the final analysis.

formula for the radio-loudness is given as:

$$\mathcal{R} = \log_{10}\left(\frac{L_{144\,\mathrm{MHz}}/\mathrm{W\ Hz^{-1}}}{L_i/\mathrm{W\ Hz^{-1}}}\right) \tag{2}$$

Where $L_{144\,\mathrm{MHz}}$ is the luminosity of a quasar at a frequency of 144 MHz and $L_{i-\mathrm{band}}$ is the luminosity of a quasar at a frequency of ∼393 THz (= 7625 Å), which is the central frequency of the SDSS i-band. In order to calculate the i-band luminosity from the absolute magnitudes, a k-correction must first be applied. The SDSS DR16 quasar catalog has its absolute magnitudes of the i-band k-corrected to z = 2. To correct these magnitudes for the extinction, meaning correcting them to z = 0, the following formula is applied, taken from Richards et al. (2006):

$$M_i(z=0) = M_i(z=2) + 2.5(1+\alpha)\log(1+z) \tag{3}$$

Here $M_i(z=0)$ is the k-corrected absolute i-band magnitude to a redshift of zero, $M_i(z=2)$ the absolute i-band magnitude as given in the SDSS DR16Q catalog, z the redshift of a quasar and α the optical spectral index. For the i-band, the calculations use $\alpha = -0.5$, the canonical value for the spectral index (Richards et al. (2006)). From the k-corrected magnitude the luminosity of the selected quasars can be calculated using solar constants: magnitude ($m_\odot$) and luminosity ($L_\odot$). The conversion is given by the formula:

$$L_i = L_\odot \times 10^{-0.4(M_i - m_\odot)} \tag{4}$$

Here L_i represents the luminosity of the i-band in Watts, $L_\odot$ the solar luminosity constant, M_i the k-corrected absolute i-band magnitude calculated with formula 2, and $m_\odot$ the solar apparent magnitude. Obtaining the right units of W Hz^{-1}, the i-band luminosity is divided by the central frequency of the i-band. The k-correction of the radio-flux requires a different calculation. In contrast to formula 2, the new k-correction formula does not use absolute magnitudes as a variable but flux directly, as no absolute magnitude of the 144 MHz LOFAR band is presented

in the used catalogs. This new formula is formulated as the following:

$$L_\nu(\nu_0) = F_\nu(\nu_0) 4\pi D_L^2 (1+z)^{\alpha-1} \tag{5}$$

Here L_ν represents the luminosity at a specific frequency, in this case, $\nu_0 = 144$ MHz. Similar to this parameter is F_ν which gives the flux at a specific frequency (144 MHz). This is the flux as given in the LOFAR catalogs, but in this case, converted to W m^{-2} to obtain the final L_ν in W Hz^{-1}. D_L is the luminosity distance and z represents the redshift of each quasar. The spectral index is given as $\alpha = 0.7$, as found in Hardcastle et al. (2016). Having found both the luminosity parameters in formula 2, a radio-loudness can be calculated and a check whether an actual dichotomy exists can be done.

3.2 SED fitting with CIGALE

As mentioned in the introduction, the previously mentioned method has been conducted many times and no dichotomy was found. That is why in this study, a further fine-tuning of the radio data is employed. The goal of the fine-tuning is to separate the radio luminosity into two components: the component of the AGN radio emission and the radio emission from star formation. In the end, the radio-loudness of solely the AGN component is taken as to rightfully determine whether a quasar dichotomy in the radio waveband exists.

The separation of the two radio emission components was achieved by subtracting data from modeled SEDs, using CIGALE, a multiwavelength SED fitting code (Boquien et al. (2019)) with an improved fitting mechanism by Yang et al. (2022). The code is able to take multiwavelength data from different observation bands as input. The passbands with which the SED models for the quasar sample are created are already mentioned in the Data section, but for overview are listed in table 2. The content of the dataset required to run CIGALE must include a quasar id, redshift, and flux data. This data along with their errors should be passed along in units of mJy. As x-ray data is mostly given in cgs units of ergs s^{-1} cm^{-2}, a conversion to flux units of mJy, given by Yang et al. (2020), can be done in the following:

$$F(\text{Jy}) = \frac{F_x \times 4.136 \times 10^8}{E_{up} - E_{lo}} \tag{6}$$

Here F(Jy) is the flux in Jy, F_x the x-ray flux in ergs s^{-1} cm^{-2} as obtained from the original dataset, and finally E_{up} and E_{lo} are the upper and lower energy limit of the x-ray band in units of keV.

Some quasars lack data in specific columns due to faulty observations or simply because this data is not cross-matched. This is the case for many quasars in the x-ray bands, as these datasets were not cross-matched but added onto the existing dataset. Fortunately, lacking data does not pose an issue for CIGALE. SED modeling can therefore proceed without fault. With the dataset, a configuration file is needed to be prepared. This file contains information on the quasar properties within the dataset. Different parameters are divided into modules that correspond to a physical property or process of the objects. These modules are a crucial element for SED modeling, as they progressively compute every model. The sequence of the utilized modules to compute each SED model is the following:

1. The computation of the star formation history (SFH) of each quasar.
2. The computation of the stellar spectrum and the single stellar population models.
3. The computation of the nebular emission. These are calculated from the Lyman continuum photon emission.

4. The computation of the amount of luminosity absorbed by dust, assuming an attenuation law.
5. The computation of dust emission in the MIR and FIR, accounting for energy balance. This means that energy absorbed by dust at short wavelengths (computed in step 4) is re-emitted at longer wavelengths.
6. The computation of the emission produced by the AGN.
7. The computation of x-ray emission from both the AGN and the host galaxy combined.
8. The computation of radio emission from both the AGN and synchrotron emission.
9. The redshifting of the model, including a computation of the absorption due to the inter-galactic medium (IGM).

For the SFH computation, CIGALE offers a range of modules. The difference between each module lies in the different methods of SFH modeling. For example, the SFH can be calculated as two decaying exponential models but also as a periodic model. For this project, I chose the SFH module `sfhdelayed`. This module models a "delayed" SFH, given by:

$$\mathrm{SFR}(t) \propto \frac{t}{\tau^2} \exp\left(\frac{-t}{\tau}\right) \text{ for } 0 \leq t < t_0 \tag{7}$$

Here t_0 represents the current age of the SF, taking its commencement as zero-point, and τ is the time at which the SFR peaks. This function results in almost a linear increase starting at the t_0 and smoothly decreases after peaking at $t = \tau$. Parameters available for input include the age of the stellar population and e-folding times. Both the main stellar population and the late starburst population allow for parameter input. The mass fraction of the late burst population can be set manually as well. After having computed the SFH, an intrinsic stellar spectrum is modeled. Here, the module `bc03` is utilized, extracted from a single stellar population (SSP) library (Bruzual and Charlot (2003)). For the modeling The module requires three parameters only: the initial mass function (IMF), the metallicity, and the separation age between the young and the old star populations. At this stage, the stellar populations are dust-free. The spectra are therefore not attenuated by potential reddening. This attenuation will be accounted for in the dust attenuation module. Because this can not be done immediately, as the nebular emission module follows first, the spectra of old and young stars are stored separately. As already mentioned, the SSP module is followed by the nebular emission module (`nebular`). Nebular emission is a result of the following: Lyman continuum photons originating from stars are able to ionize the surrounding gas, which re-emits the energy. The module is based on the nebular templates from Inoue (2011). Parameters present in this module include the ionization parameter and the metallicity of the gas. Following `nebular`, the dust attenuation is computed. This module must be able to model dust attenuation properly. This is because the energy absorbed from the UV to the NIR is re-emitted in the MIR and FIR. A proper energy balance is therefore crucial. For the modeling of this dust attenuation, I chose the module `dustatt_modified_starburst`. This module is based on the starburst attenuation curve realized by Calzetti et al. (2000). Most parameters within this module are kept at their default value given by CIGALE. One parameter on the other hand $E(B-V)_{\mathrm{lines}}$ was given a range of values. This parameter represents the reddening of the emission lines. Next, the dust emission module is implemented. Just like the attenuation module, modeling the dust emission takes into account energy balance too. For this project I chose the module `dale2014`, based on the IR dust templates from Dale et al. (2014). After the computation of the dust effects on the SED, the AGN component is modeled. For

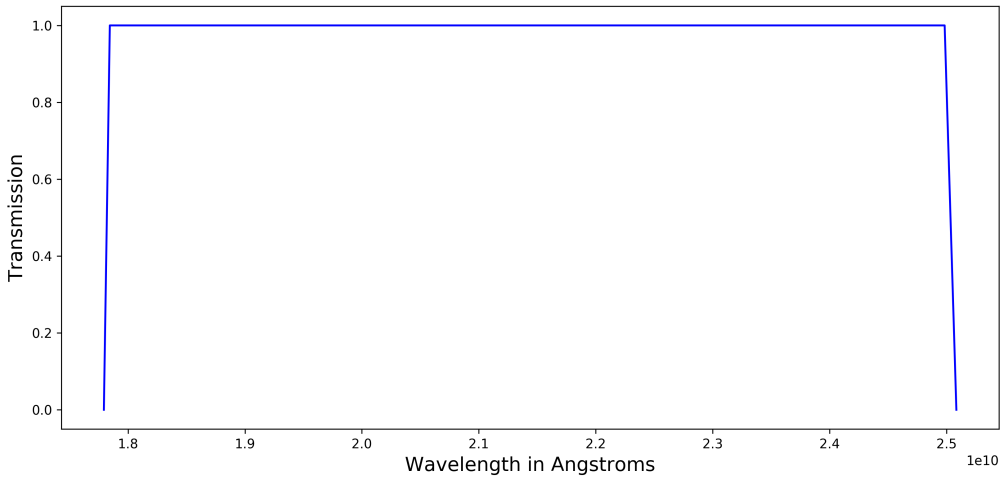

Figure 9: Boxcar filter of the 144 MHz LOFAR band created for the CIGALE data processing. Wavelength is given in Å.

this task, I chose the `skirtor2016` module, based on the clumpy torus model (Stalevski et al. (2012), Stalevski et al. (2016)). Parameters relevant for the final data output from this module were $frac_{\mathrm{AGN}}$ and $\lambda_{frac_{\mathrm{AGN}}}$. The latter represents the range in microns at which to calculate the AGN contribution to the total SED. This contribution was rounded to the values given for the parameter $frac_{\mathrm{AGN}}$. The following modules were the `xray` and the `radio`, crucial for the SED to be modeled at these wavelengths. Finally, the last module in the configuration file to contribute to modeling the SEDs is `redshifting`. This module has two functions affecting the SED. The first effect is the redshifting and dimming of the spectrum, multiplying the wavelengths by $1+z$ and dividing the spectrum by $1+z$. The other function takes into account the short wavelength absorption by the IGM, prescripted by Meiksin (2006). For the SED fitting, the code requires an identification of each band used for analysis. Most of these bands were already available for use in CIGALE, with only some x-ray bands and the LOFAR 144 MHz bands missing. For these missing bands, "boxcar" bands were created, having maximum transmission (equal to one) in the wavelength range of the bands, and a rapidly decreasing to zero transmission otherwise. All filters have their wavelength measured in Å. As an example, the 120 - 168 MHz LOFAR filter created is presented in figure 9.

With the dataset and the configuration file set up, the code can model SEDs for every object in the dataset and can return the best-fitted SED for each object, along with its χ^2 value. From the 1154 best-fitted SEDs only those with a $\chi^2 < 5$ and a non-zero dust luminosity are selected for the final data analysis, as the SEDs which do not meet this requirement can produce inaccurate results. Both example plots of selected and discarded quasar plots can be found in the Appendix. Examples of included SED models are shown in Figure 20, whereas examples of discarded models are shown in Figure 21. Alongside the SEDs, CIGALE can provide not only flux and luminosity data from the SEDs but data on the star formation (SFR) per quasar as well. Other quasar properties are taken from an external dataset (Wu and Shen (2022)).

3.3 Removing the star formation component from the radio-loudness

With the returned SEDs and quasar properties from CIGALE, the SF component of both the i-band and 144 MHz luminosity can be discarded. For the i-band luminosity, this is done in the following way: As mentioned in section 3.2, an AGN fraction of the total flux in the optical i-band is estimated for every quasar in the sample. Having obtained the calculated i-band luminosity by formulas 3 and 4, the SF component was removed by simply multiplying each fraction with the i-band luminosity for each quasar.

Removing the non-AGN component for $L_{144\ \mathrm{MHz}}$ on the other hand took a more sophisticated approach, as radiation from thermal SF does not exist in the radio. Using an AGN fraction as for L_i to obtain the radio component of AGN only is therefore impossible. As mentioned in the Introduction, the method to obtain the AGN component of $L_{144\ \mathrm{MHz}}$ is done by converting the total infrared (TIR) to $L_{144\ \mathrm{MHz}}$ utilizing the Far-infrared Radio Correlation (FIRC). What should be noted, is that the FIRC evolves with redshift as a consequence of Cosmic Microwave Background (CMB) effects (Murphy (2009)). This property affects the linearity of the FIRC and therefore the conversion process at high redshifts. For this reason, only the quasars with $z < 3$ were selected for further data analysis.

The process of separating SF from the total radio luminosity was conducted by fitting a line to the scattered data of $L_{144\ \mathrm{MHz}}$ versus the total luminosity of the dust (L_{TIR}) obtained from CIGALE, divided by a frequency of 3.75×10^{12} Hz to account for conversion in identical units. The plot along with the best-fitted line is given in figure 10. As the scales of the correlation are logarithmic, the luminosity conversion is given as $L_{144\ \mathrm{MHz}} = 10^{a_{\mathrm{best}} L_{\mathrm{TIR}} + b_{\mathrm{best}}}$, with a_{best} the best-fitted slope and b_{best} the best-fitted $L_{144\ \mathrm{MHz}}$-intercept. The best-fitted parameters a_{best} and b_{best} were determined with the Python module `scipy.optimize.curve_fit`. To account for the error

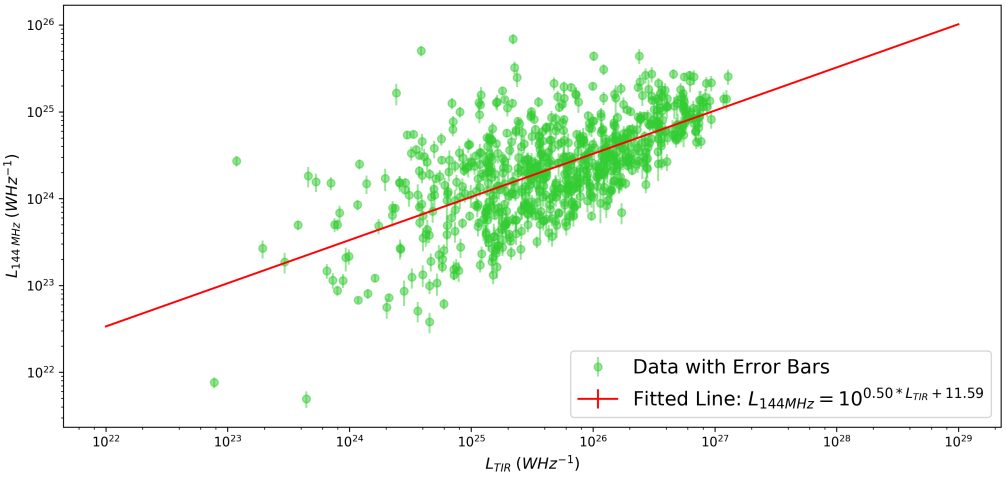

Figure 10: The FIRC along with the best-fitted line. The values of the best-fitted parameters rounded to two decimals are $a_{\mathrm{best}} = 0.50 \pm 1.20$ and $b_{\mathrm{best}} = 11.59 \pm 30.88$. Error bars are only shown for $L_{144\ \mathrm{MHz}}$. These errors are given in every LOFAR catalog used. L_{TIR} on the other hand does not have an error as this was not included in the CIGALE output. Therefore, it is assumed that L_{TIR} does not have an error.

in the best-fitted parameters and to increase the quality of quasar selection, a Gaussian sampling method was applied. This method utilizes a randomly generated Gaussian with the mean set

Telescope	Bands
SDSS	u (3543 Å), g (4770 Å), r (6231 Å), i (7625 Å), z (9134 Å)
LOFAR	144 MHz band*
Herschel (SPIRE and PACS)	PSW (250 μm), PMW (350 μm), PLW (500 μm), green band (100 μm), red band (160 μm)
WISE	WISE1 (3.37 μm), WISE2 (4.62 μm), WISE3 (12.08 μm), WISE4 (22.19 μm)
XMM-Newton	0.2 - 12 keV total flux*
Chandra	0.5 - 7 keV, 0.5 - 2 keV, 2 - 7 keV
eROSITA	0.2 - 2.3 keV*

Table 2: Telescopes along with their respective bands used in CIGALE. *These are manually created "boxcar" filters and separately added to the CIGALE code.

at a_{best} and $\sigma = \sqrt{\sigma^2_{\text{best}}}$. Here σ^2_{best} is the covariance found with `scipy.optimize.curve_fit`. From this Gaussian 500 samples were taken. For every sample $L_{144\text{ MHz}} - 10^{a_{\text{sample}} L_{\text{dust}} + b_{\text{best}}}$ was calculated, where a_{sample} was substituted for each value in the Gaussian. Looping over all Gaussian samples, a matrix with the dimension of 732×100 was formed. From this matrix, a new matrix was created, grouping the number of iterations, thus inversing the matrix, making the dimension 100×732. The negative arrays along with the individual negative results were discarded. These quasars are labeled as being completely dominated by radio luminosity from SF and were thus not included in calculating the distribution of $\mathcal{R}$, having a negligible AGN component. After excluding the negative values, the arrays could end up having varying lengths. As a result, for each remaining array, a normalized histogram for $\mathcal{R}$ was created, and afterward, the average of all 100 histograms was taken. This error analysis allows the error of the FIRC to be incorporated within the final distribution of the radio-loudness parameter, optimizing the accuracy of the final result.

Once having obtained the distribution of the radio-loudness, the parameter will be plotted against other quasar properties: redshift, bolometric luminosity, black hole mass, and $\lambda_E dd$. These properties are taken from a quasar property catalog, made to accompany the SDSS DR16Q catalog Wu and Shen (2022). All plots will be presented in section 4. If a significant correlation exists between $\mathcal{R}$ exists, then a best-fitted line is calculated as well, using `scipy.optimize.curve_fit`, similar to the fitting process for the FIRC.

4 Results

As to compare the results of a non-separated radio-loudness and a radio-loudness that is, the $\mathcal{R}$ is presented four times, accounting for every combination of the $L_{144\text{ MHz}}$ to L_i ratio. First of all, $\mathcal{R}$ is calculated without accounting for the SF component. This result is portrayed in Figure 11. Along with the histogram showing the distribution, two Gaussian curves were fitted to see where potential peaks of RQ or RL quasars are contained within the distribution. The mean of these curves is presented as well. From the histogram and the curves, no distinct bimodality can be extracted. The result looks exceedingly similar to $\mathcal{R}$ as found by Gürkan et al. (2019). The Figure agrees with this research, as the RL quasars are indeed a continuous extension from the RQ, made visible by the smooth total Gaussian curve, exhibiting no bumps.

After the finding of this result, the data analysis proceeded to use CIGALE for the two-component separation of the radio-loudness. The initial values can be found in the Appendix. The number of models calculated for 1154 quasars yielded a total of 225,854,720 models (203,840 per redshift). Excluding the best-fitted SEDs that have a χ^2 larger than 5, the final data set is

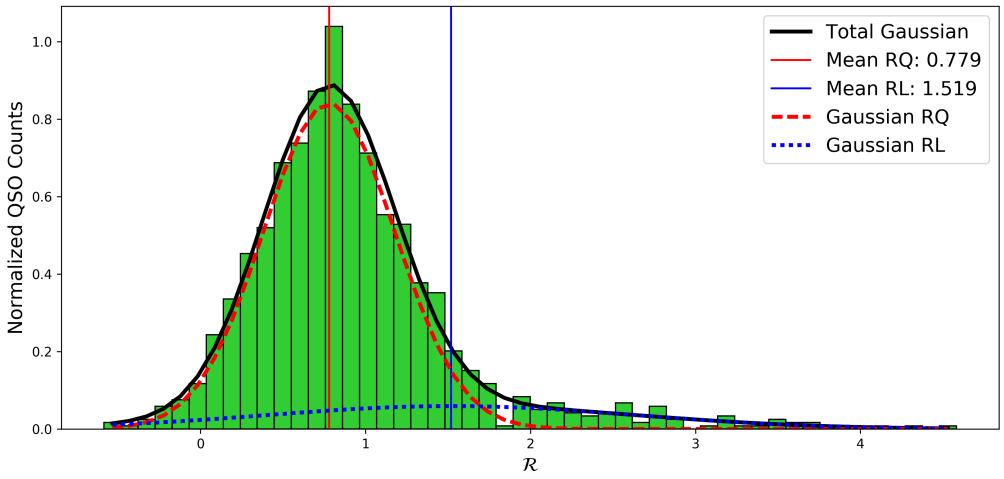

Figure 11: Distribution of the radio-loudness $\mathcal{R}$. This radio-loudness is a combined ratio of SF and AGN. Separate peaks showing a potential dichotomy are shown by two Gaussian curves, with their mean presented as a vertical line. By the shape of the curves, no obvious separation is present.

left with 732 QSOs. From the CIGALE output, the AGN fractions in the i-band were extracted and multiplied by the k-corrected i-band luminosity to account for the SF contribution and other potential sources producing emission observed in the i-band. Accounting for only the SF contribution within the modeled flux of the i-band produces a $\mathcal{R}$ distribution displayed in Figure 12. Unlike Figure 11, this distribution has a slight bump around a $\mathcal{R}$ of approximately 2, hinting at a potential dichotomy. Apart from the difference in the shape of the two best-fitted curves, the overall distribution of quasars has changed as well. The distribution is shown to be more spiky. Where the radio-loudness exhibits a distinct peak in Figure 11, Figure 12 on the other hand has at its center three peaks. The Gaussian mean for the RQ quasars has somewhat shifted to the right, meaning a more overall RL distribution. After the two-component separation of L_i, I separated the $\mathcal{R}$ completely by subtracting the fitted radio luminosity from the total L_{144}. The result is given in Figure 13. The $\mathcal{R}$ does not look very different from Figure 12. The only visible difference is a slight change in μ for both Gaussians, having shifted a bit to the RL end of the distribution. Figure 14 presents the overlapped distribution to aid in visualizing the difference. The distribution where $\mathcal{R}$ is fully separated appears to be more RL. This is displayed by a larger quasar count at approximately $\mathcal{R} > 1.5$. Moreover, a slight increase in RQ quasars at approximately $\mathcal{R} < 0$ is present. As described in the methods, I use samples from a randomly distributed Gaussian to calculate the final result. Because of the randomly extracted samples, the $\mathcal{R}$ distribution varies per Gaussian. Examples of different result comparisons are shown in the Appendix. Overall, the same pattern occurs. The distribution shows more quasar counts at higher values of $\mathcal{R}$. Because of the differing distributions, one distribution was chosen to relate to the quasar properties. This was done to avoid differing results per run, avoiding a large range of differing results in the Appendix.

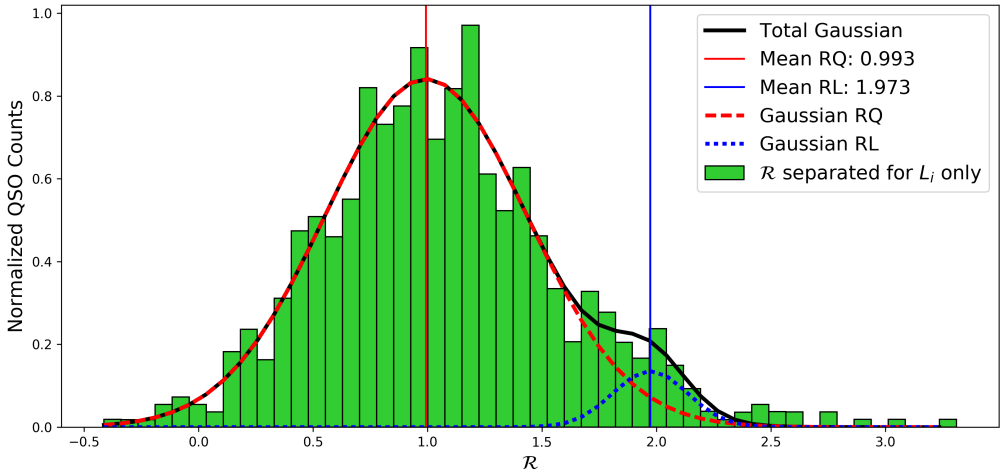

Figure 12: Distribution of $\mathcal{R}$. The luminosity component due to SF is removed from L_i. Separate Gaussian curves are shown along with the total Gaussian. The blue-dotted Gaussian shows a small bump and potentially hints towards the presence of a dichotomy.

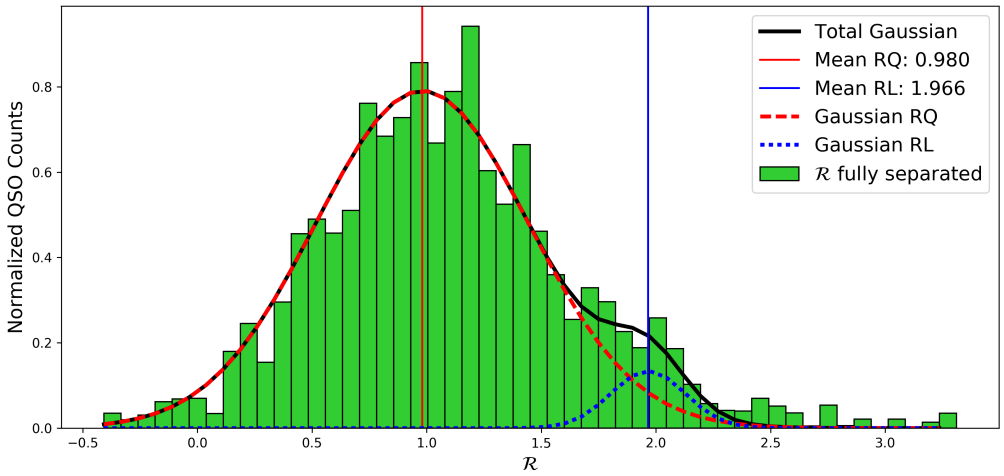

Figure 13: Distribution of $\mathcal{R}$. The luminosity from the SF component is removed from both L_{144} and L_i. Separate Gaussian curves are shown along with the total Gaussian. The blue-dotted Gaussian shows a small bump and potentially hints towards the presence of a dichotomy. The result is similar to Figure 12.

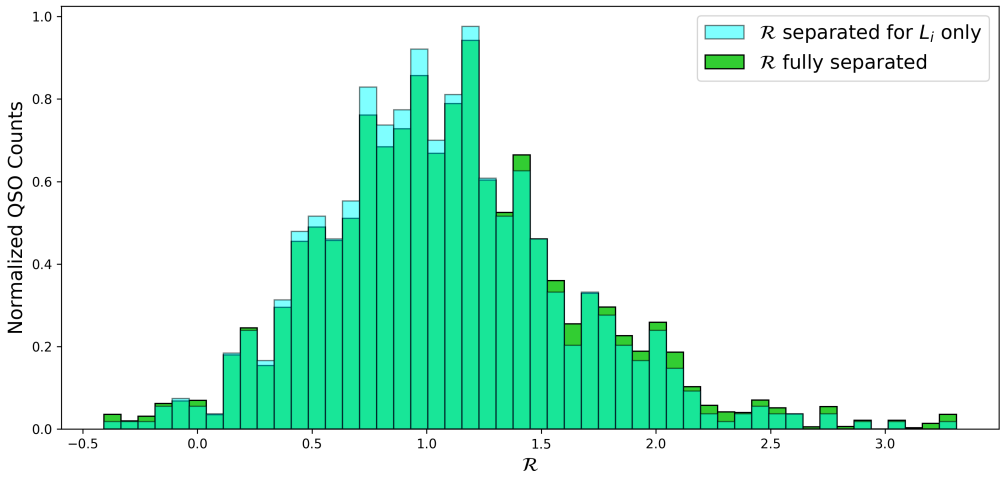

Figure 14: Two distributions of the radio-loudness $\mathcal{R}$. The cyan distribution is the same distribution given in Figure 7. The green $\mathcal{R}$ distribution represents the SF removed $\mathcal{R}$ from both L_i and $L_{144\text{ MHz}}$

4.1 Relationships between $\mathcal{R}$, z, and other quasar properties

Having established the final radio-loudness distribution accounting for star formation in both the $L_{144\text{ MHz}}$ and L_i, it can now be investigated whether this parameter has any significant correlation or relationship with quasar properties. The properties under investigation are z, bolometric luminosity, SFR, black hole mass, and finally the Eddington ratio. In Figure 15, the radio-loudness is given as a function of z. The distribution seems overall flat, following no obvious inclination. The distribution is mostly dominated at $\mathcal{R} \approx 1$, where most of the quasars lie. This is therefore no surprise. Nevertheless, Spearman's correlation coefficient along with the p-value was calculated to statistically determine the potential presence of a correlation. From the Spearman test, I obtained $r_s = 0.13$ and p-value 0.00027. Coefficients and p-values for all relationships investigated are listed in table 3. All values are rounded to two decimals unless smaller than 5 orders of magnitude. In this case, only the order of magnitude is given. Figure 16 shows the relationship of $\mathcal{R}$ as a function of bolometric luminosity (L_{bol}). Already by visual inspection, a negative correlation seems to be apparent. This anti-correlation is given by $r_s = -0.37$ with a p-value $\sim 10^{-25}$. Moving on to the SFRs of each quasar in Figure 17, a linear relationship seems less apparent compared to the $\mathcal{R}$ to L_bol relationship. A notable property, however, is that the distribution shows that the quasars with the largest values of $\mathcal{R}$ do not seem to have low SFRs, opposing the RQ majority which tends to have lower SFRs. The data displays a correlation, having $r_s = 0.29$ and a p-value of $\sim 10^{-15}$. The display of $\mathcal{R}$ as a function of the black hole mass is done in two separate Figures, due to two different measuring methods of the black hole mass: using MgII lines, or CIV lines. The results are given in Figure 18. The data set providing the data on black hole masses has multiple lacking data points, given by a zero (Wu and Shen (2022)). These data points were excluded from the plot and the Spearman coefficients along with the p-values were only calculated for the non-zero black hole masses. The relationship between $\mathcal{R}$ and black hole mass measured using MgII lines yields $r_s = -0.21$ with p-value $\sim 10^{-8}$. Using CIV lines these values change to $r_s = 0.000079$ with p-value $= 0.99$. The incredibly large p-value could be a reason for a lack of data points, which is likely a result of

Quasar property relationship	Spearman's correlation coefficient r_s	P-value
z and $\mathcal{R}$	0.13	0.00027
Bolometric luminosity and $\mathcal{R}$	-0.37	10^{-25}
Star formation rate and $\mathcal{R}$	0.29	10^{-15}
Black hole mass (MgII) and $\mathcal{R}$	-0.26	10^{-10}
Black hole mass (CIV) and $\mathcal{R}$	0.00079	0.99
Eddington ratio and $\mathcal{R}$	-0.17	10^{-6}

Table 3: Results of Spearman's correlation coefficient per relationship between $\mathcal{R}$ and a quasar property.

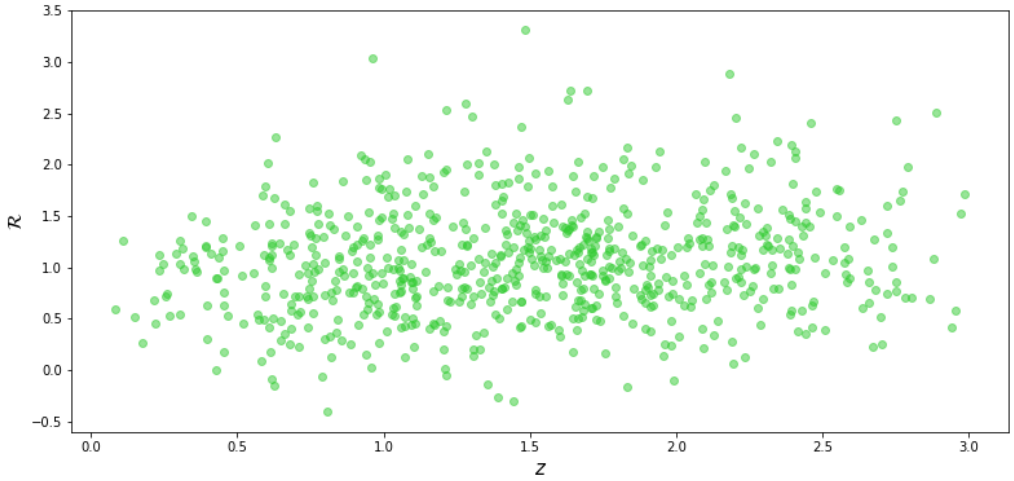

Figure 15: Distribution of $\mathcal{R}$ as a function of z.

disadvantageous measurements due to the large z. The final investigation is of the Eddington ratio. $\mathcal{R}$ as a function of λ_{Edd} tends to cluster to form a correlation but on the other hand has outliers that do not follow this pattern at all. Nevertheless, $r_s = -0.17$ and the p-value is quite low: 10^{-6} approving of a weak anti-correlation.

5 Discussion

This section contains a summary of the results found in this thesis, along with their potential implications. First of all, the accuracy of the data is discussed. This discussion regards the CIGALE input as the major cause of the error. Afterwards, the results and implications on the fully separated $\mathcal{R}$ distribution is discussed. Lastly, a discussion regarding the relationships between $\mathcal{R}$ and the quasar properties is held.

5.1 The accuracy restrictions due to CIGALE

Before analyzing the results regarding the radio-loudness, it is necessary to assess the accuracy of the CIGALE in- and output. The CIGALE SED fitting code has been a critical source of data processing. Assessment of its performance is therefore incredibly important. The final SEDs used for calculating the separated $\mathcal{R}$ distributions are a product of the configuration file, which setup

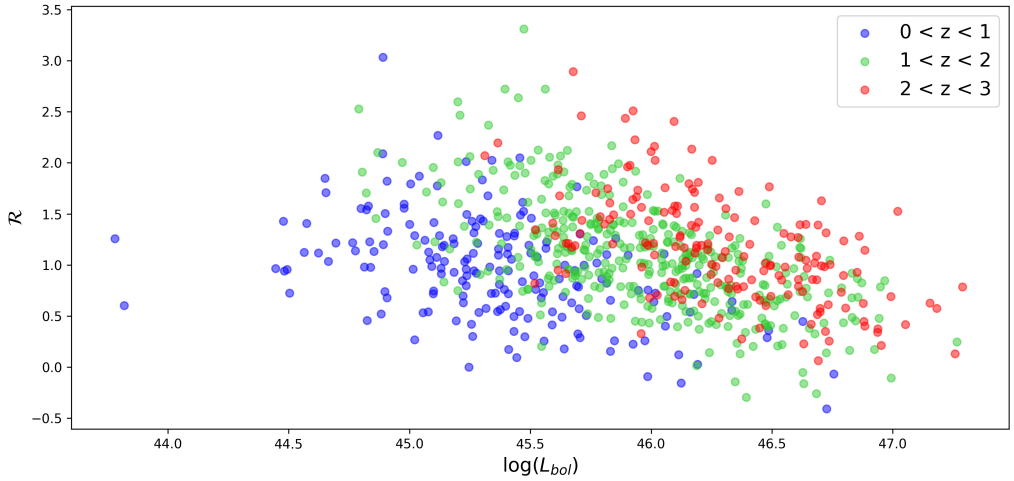

Figure 16: Relationship of $\mathcal{R}$ as a function of $L_{\rm bol}$ in Watts. Redshift ranges are given different colors.

is given in Table 4. Therefore, the accuracy assessment starts here. As mentioned in section 3.2, the number of models calculated with the configuration file was 225,854,720 (203,840 per redshift). This amount is relatively small for a data set of 1154 quasars. The small amount of models is a cause of parameter reduction. This was done on purpose to reduce computer labor. The disadvantage of this method is that the best-fitted SED models used for the data analysis reduce in accuracy. Effects of the accuracy depletion can lead to inaccurate models having low χ^2 values. Another consequence is that SED models lack dust-emission contribution. These errors result in an erroneous quasar selection. On the other hand, the reduced parameters were not the only cause of inaccurate χ^2 values. In the dataset used for this project, the flux errors for some quasars were wrongly inserted into the dataset. The consequence of this is that these SEDs have a reduced χ^2. This means that some models have $\chi^2 < 5$, even though they would not if the errors were implemented properly. Examples of "bad" models previously described are presented in Figure 21. Further disadvantages of parameter reduction are accuracy reductions in the calculations of quasar dust-emission. As described in section 3.2, the module `radio` was used to model the presence of radio emission on the SED. This module contains the parameter $q_{\rm IR}$ which represents the radio-IR correlation parameter (Helou et al. (1985)). This parameter can force an elevated IR emission if the flux in the radio is large. For this parameter, I only proposed the value 2.58 which is the default value given by CIGALE. Multiple parameters could therefore give the radio-IR correlation a more prominent role and potentially more accurate SED models could be generated. The accuracy of the SED modeling, especially in the IR range, is crucial to the data analysis. This is because the total dust-luminosity deducted from CIGALE is used for the FIRC. This data is eventually used to calculate L_{144} for the fully separated $\mathcal{R}$ distribution. Another parameter affecting the production of the final $\mathcal{R}$ distribution is the $frac_{\rm AGN}$ parameter. This parameter decides at which fractions the AGN contribution is rounded (in the i-band). For this parameter, I proposed the values: 0, 0.1, 0.2, 0.4, 0.6, 0.8, and 0.99 (see Table 4). These fractions have relatively large gaps between them. The effect of these far-spaced ranges can be seen in Figure 12. The distribution depicted here is very spiky compared to Figure 11. These spikes are likely caused by the small number of fractions to round to, resulting in the "flooding" of various bins. The smoothness of the distribution is therefore negatively impacted, increasing

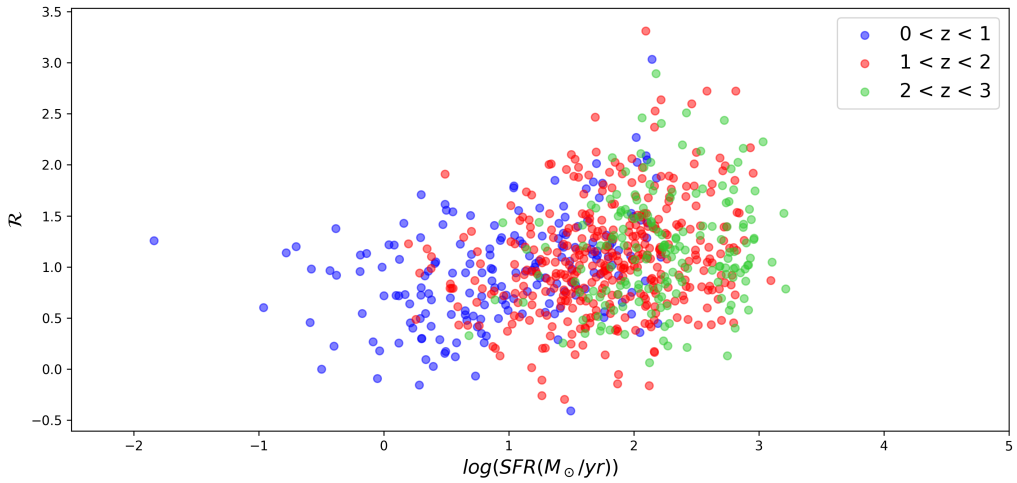

Figure 17: Distribution of $\mathcal{R}$ as a function of the SFR. Redshift ranges are given different colors.

the difficulty of determining whether a radio dichotomy for quasars is present.

5.2 Do quasars exhibit a radio-loudness dichotomy?

Figure 11 shows a wide range of $\mathcal{R}$ values, but no two distinct peaks are detectable. In this thesis, two Gaussian curves are fitted as to determine whether such peaks are present. Even with the Gaussian curves, no bimodality is made apparent. The $\mathcal{R}$ distribution shows a RQ peak at $\mathcal{R} \approx 0.8$. This peak is smoothly transitioned into the RL end of the distribution. This result is similar to the $\mathcal{R}$ distribution obtained in Gürkan et al. (2019) (see Figure 4). These similarities confirm having comparable data sets when it comes to calculating $\mathcal{R}$. In the next step, I removed the SF contribution from L_i. The result is shown in Figure 12. As can be seen from the best-fitted Gaussian curves, two distinct peaks are found. Compared to Figure 11, the RQ into RL transition is less smooth. The originally smooth transition is interfered with by a relatively small Gaussian bump, centered at $\mu \approx 1.97$ with $\sigma \approx 0.16$. The bump could be an indicator of a radio dichotomy. However, no immediate bimodality is apparent as there is no distinct minimum between the RQ and RL Gaussians. The final and fully separated $\mathcal{R}$ distribution is given in Figure 13. The fully separated $\mathcal{R}$ distribution seems extremely similar to Figure 12. The means of both their Gaussian curves are almost identical. A comparison is made in Figure 14. From this comparison, it can be seen that the fully separated $\mathcal{R}$ distribution is more RL. As mentioned in the Results, multiple results of the distribution are possible due to the random Gaussian sampling method. Figure 22 shows the possible variations as a cause of this method. Although these figures show a similar pattern, it can not be stated in what quantities the fully separated distribution becomes more RL after accounting for the SF component in L_{144}. Therefore, a claim of whether the SF separation has a significant impact on $\mathcal{R}$ can not be made. Just like in Figure 11 and 12, best-fitted Gaussian curves are plotted. Compared to 12 where only L_i has been separated, the final $\mathcal{R}$ distribution has almost identical best-fitted Gaussians. Therefore, no radio dichotomy can be clearly distinguished for the same reasons it can not be distinguished in 12. Although Figure 12 and 13 look alike, they differ slightly as can be seen in Figure 14. This Figure shows the fully separated $\mathcal{R}$ distribution to be more RL compared to

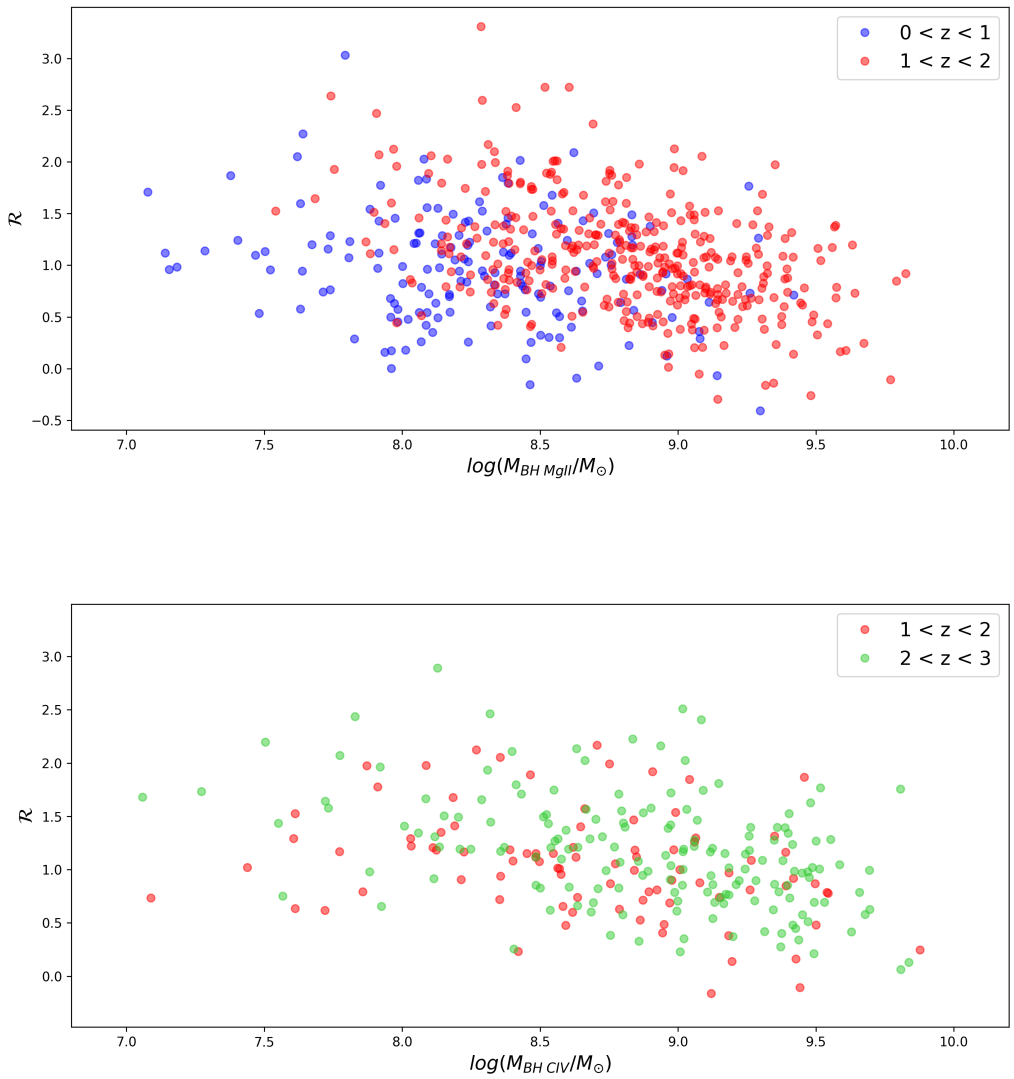

Figure 18: *Top*: Distribution of $\mathcal{R}$ as a function of black hole mass measured by means of MgII lines. *Bottom*: Distribution of $\mathcal{R}$ as a function of black hole mass measured by means of CIV lines.

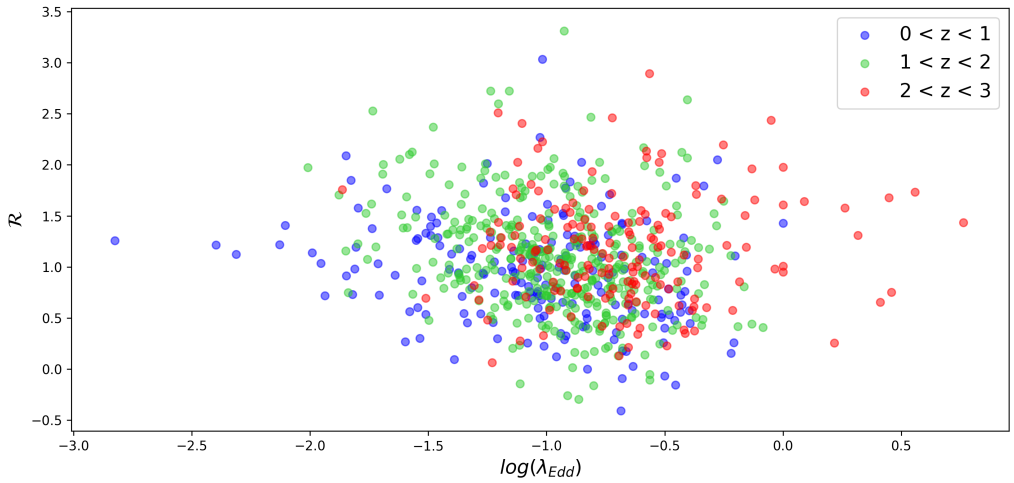

Figure 19: Distribution of $\mathcal{R}$ as a function of λ_{Edd}

the $\mathcal{R}$ distribution that is separated for L_i only. This is rather unexpected, as I expected the distribution to be more RQ. Removing the contribution from SF takes away radio luminosity, resulting in a more RQ distribution. This however is not the case. An explanation for the result presented in Figure 14 must therefore be a cause of another factor. This factor could be explained by the methods in which the distribution was obtained. As explained in the methods, a best-fitted line representing the FIRC was used to obtain the separated L_{144} component. For some quasars, this subtraction equated to negative values. Negative values indicated a quasar was completely dominated by radio emission due to SF and are therefore excluded. This exclusion leads to certain bins reducing in counts and other bins increasing. The result of this change in counts could therefore be a possible explanation for the difference displayed in Figure 14.

5.3 Does $\mathcal{R}$ correlate to quasar properties?

Table 3 shows all Spearman correlation coefficients for all quasar properties considered. Most correlation coefficients indicate a weak correlation. Looking at the p-values, the correlation of $\mathcal{R}$ between z and the black hole mass measured with CIV lines appears to be relatively large. The correlation between $\mathcal{R}$ and the black hole mass (CIV) is refuted due to the large p-value of 0.99. The reason for this large p-value is probably a consequence of the lack of data points. Not every quasar in the left-over sample had a measured black hole mass. For the black hole masses that were measured with CIV, this amount dropped even more. This lack of data points is most likely the factor that increased the p-value, as the scatter of the data points is too large in comparison to the correlation. For z on the other hand the p-value is quite small, yet not as small compared to the other values. By the definition of the p-value, the correlation has a large chance of not being random. Although this is true, the small value of r_s already indicates a very weak correlation. Looking at 15, the distribution seems to be quite random and is thought to be a coincidence due to the majority of the quasars to lie at $\mathcal{R} \approx 1$. Therefore, a potential correlation between $\mathcal{R}$ and both z and the black hole mass measured with CIV lines are in doubt. I continue my correlation analysis to $\mathcal{R}$ as a function of L_{bol} shown in Figure 16. Spearman's correlation coefficient of this relationship indicates a moderate anti-correlation. Moreover, the p-value is incredibly small: 10^{-25}. By eye, this correlation seems to be apparent as well. From

what it seems, the correlation appears to be linear. This anti-correlation is not self-explanatory, as $L_{\rm bol}$ is determined by the accretion rate onto the central supermassive black hole (SMBH) and is related to the overall energy release from the accretion process (e.g. Bian and Zhao (2003), Körding et al. (2007)). Radio-loudness on the other hand is influenced by the presence and strength of relativistic jets. The anti-correlation can signify various implications. First of all, the anti-correlation between $\mathcal{R}$ and $L_{\rm bol}$ could indicate that the formation and/or maintenance of relativistic jets is energetically challenging: When the overall energy output produced by the AGN increases, the efficiency of relativistic jet creation decreases. Secondly, as previously mentioned, the bolometric luminosity of AGN is related to the SMBH accretion rate. Moreover, bolometric luminosity is found to correlate with black hole mass (Xie et al. (2004)). Therefore, the anti-correlation could imply that higher accretion rates or larger black hole masses tend to be associated with a lower $\mathcal{R}$. This claim is supported by the correlation coefficient found for the relationship between $\mathcal{R}$ and the black hole mass measured using MgII lines shown in Figure 18. For this relationship $r_s = -0.26$ with a p-value of the order of 10^{-10}, meaning the anti-correlation is not likely to be random. The anti-correlation between $\mathcal{R}$ and the black hole mass could suggest that the formation and maintenance of strong relativistic jets are more common in AGNs with lower black hole masses. However, this claim can not be made with certainty as the source of radio jets is still a debated topic (see section 1.1). Moreover, the correlation coefficient of the relationship between $\mathcal{R}$ and the black hole mass is quite small. This correlation is therefore very weak and the black hole mass might therefore not be dependent on $\mathcal{R}$, regardless of what the p-value is. The next relationship to analyze is between $\mathcal{R}$ and the final nuclear property: λ_{Edd} shown in Figure 19. This relationship was found to be weakly anti-correlated. Comparable to the correlation coefficient for the black hole mass (MgII), the Eddington ratio could too be a coincidence of most quasar counts being situated at $\mathcal{R} \approx 1$. This claim can be supported by the large scatter of $\lambda_{\rm Edd}$, contradicting a clear anti-correlation.

5.4 Evolutionary stages of the quasars

The final relationship to be evaluated is the relationship between $\mathcal{R}$ and the SFR, shown in Figure 17. Unlike the other relationships (excluding the two most likely coincidental correlations) this is a correlation rather than an anti-correlation. The correlation suggests a larger SFR for radio-loud quasars. In fact, the Figure shows that most radio-loud quasars only have SFRs that are relatively large. The correlation could reflect evolutionary stages in quasars. This claim is based on a coevolution model of galaxies and their SMBH (Cen (2012)). This model states that coevolution has three distinguishable stages. The first stage initiates in a starburst period. This initial period is characterized by a high SFR and a slightly increasing SMBH mass. After this stage comes the SMBH prime period. In this period the post-main-sequence stars formed in the starburst period start to return their gas to the interstellar medium (ISM). The SFR decreases. The returned gas is now fuelling the SMBH accretion. With time, the SMBH grows while $\lambda_{\rm Edd}$ decreases. Eventually, the coevolution reaches the quiescent bulge stage. In this stage, the bulge of the galaxy is completely red and dead. Both SMBH accretion and SF have ceased. Following this model and applying it to the quasars analyzed in this project along with their respective correlations to $\mathcal{R}$, it can be deduced that RL quasars could be in the earliest evolutionary stage whereas RQ quasars could be in the SMBH prime growth stage and beyond. The reasoning behind this claim is extracted from the inferred (anti-)correlations between $\mathcal{R}$ and the SFR, black hole mass, and the $\lambda_{\rm Edd}$. The characteristic of the earliest stage, the starburst period, are all portrayed by the RL quasars in the aforementioned relationships. RL quasars have the largest SFR (by correlation), the smallest black hole mass, and the lowest $\lambda_{\rm Edd}$ (by anti-correlation). With time, and thereby with decreasing $\mathcal{R}$, the SFR decreases, and the black hole mass increases

along with λ_{Edd}. This portrays the SMBH prime period and beyond. This model is also able to explain the larger quantity of quasars that are RQ, as the early starburst phase is relatively short in comparison to the SMBH prime growth stage. According to Cen (2012) the starburst stage usually lasts approximately 0.1 Gyr. Assuming this stage is dominated by RL quasars, the short time explains why RL quasars are therefore much less abundant compared to the RQ quasars within the quasar sample.

6 Conclusion

In this thesis, the quasar dichotomy debate was revisited. As made clear in the introduction, whether a radio dichotomy for quasars exists remains undecided. Some studies found no dichotomy (e.g. Cirasuolo et al. (2003), Gürkan et al. (2019), Macfarlane et al. (2021)) whereas others have (e.g. Kellermann (1964), Ivezić, Ž. et al. (2002)). The goal of the thesis was to clear up this debate by using recent data surveys providing highly accurate data. In particular, the radio surveys obtained by LOFAR provide datasets with unprecedented angular resolution and sensitivity (see Section 2.2). These improved datasets allow the radio-loudness parameter $\mathcal{R}$ to be more refined. This thesis aimed to calculate the radio-loudness but instead of utilizing the complete quasar luminosity, the SF component was removed. The reason for this separation was to advocate a more just radio-loudness distribution, as the result of removing the SF component yielded a distribution represented by AGN only. Results of the radio-loudness distribution and the deduction of whether a dichotomy exists differ per study. This is because of the following reasons. The first reason is that the classification of RL and RQ quasars differ per paper. Furthermore, the definition of radio-loudness allows for different bands to be used. Mostly $\mathcal{R}$ is defined as the ratio of the luminosity in some radio bands divided by the luminosity in some optical bands. These bands differ per study as well. The final reason has to do with the sample used for data analysis. Size and z are able to affect $\mathcal{R}$, and therefore too the determination of the dichotomy. Because of the different effects these differences pose, this project is compared to a radio-loudness study by Gürkan et al. (2019). The reasons to compare it to this study are that the paper is fairly recent. The quasar sample analyzed in this paper uses the same high-quality LOFAR datasets to deduct the radio-loudness. Because I compared results to this paper, I chose the same definition of $\mathcal{R}$ as well. This was the logarithmic ratio of the radio luminosity at 144 Mhz divided by the i-band luminosity, obtained from the SDSS dataset. The procedure of calculating the radio-loudness parameter was done in the following way: First, data from several observational fields were cross-matched to include data from optical, infrared, radio and x-ray bands. Observations for this data were done with various telescopes. Cross-matches were performed to the LOFAR coordinates, as they were the most precise. Continuing, the cross-matched data set was first used to calculate the $\mathcal{R}$ distribution just as Gürkan et al. (2019). This was done to realize the changes the SF separation method could offer. Afterward, the data set was used to model a SED for each quasar in the sample by using CIGALE, a multiwavelength SED fitter. The results from the best-fitted SED models allowed me to separate the AGN component in the i-band. The SF separation in the 144 MHz radio band took a more sophisticated approach. For this approach the FIRC was utilized, allowing me to convert the dust luminosity obtained by CIGALE to be converted into radio luminosity. The obtained radio luminosity due to star formation was then subtracted from the total and the finalized $\mathcal{R}$ distribution was calculated.

The results obtained in this thesis indeed show a differing distribution when separating the SF from the AGN in both the 144 MHz radio band and the optical i-band. The distribution is shown to increase its overall radio-loudness. Additionally, its previously continuous tail, which transitions from the RQ to the RL side now portrays a bump. When two Gaussians are fitted

to this new radio-loudness, two Gaussian are shown to be fitted to the data. One large one for the RQ peak and one for the RL peak. Although having found distinct peaks, no solid claim of a radio-loudness dichotomy could be made. This is because there was no evident minimum between the two Gaussian curves, but rather a smooth transition. The smaller Gaussian curve causing the bump could be hinting towards a radio-loud population but it can not be concluded with certainty for this to be the case. Therefore, I conclude to have found no quasar dichotomy of the radio-loudness. However, I do not deny its existence as the obtained result does portray bimodal behavior.

Having found the SF separated $\mathcal{R}$ it was investigated whether this parameter is found to be a function of several quasar properties. Spearman's correlation coefficients along with their p-value were calculated in order to determine whether these properties are dependent on $\mathcal{R}$. Quasar properties investigated were the redshift, bolometric luminosity, SFR, and black hole mass measured by means of MgII and CIV lines respectively, and lastly λ_{Edd}. The relationships were mostly shown to weakly correlate or anti-correlate with each other. The only relationship that showed a large p-value was that between the $\mathcal{R}$ and the black hole mass measured by means of CIV lines. This result was likely because of the small number of valid data points within the sample. The relationship between $\mathcal{R}$ and the black hole mass measured with MgII lines on the other hand did show a weak correlation. Another relationship with a low p-value was the relationship between $\mathcal{R}$ and the redshift. The correlation coefficient was quite small and although the p-value was low enough to conclude a valid correlation, the dependence of redshift on the radio-loudness was still rejected, as the correlation is likely a coincidence as a result of the spread of $\mathcal{R}$. Although most relationships with $\mathcal{R}$ displayed a relatively weak correlation, one relationship was shown to be moderately anti-correlated. This relationship was between the $\mathcal{R}$ and the bolometric luminosity. The anti-correlated dependence might indicate physical attributes intrinsic to the quasar. The first attribute could be that when the overall energy output produced by the AGN increases, meaning an increase of L_{bol}, the efficiency of relativistic jet creation decreases. Another implication of the anti-correlation could be that quasars with a lower $\mathcal{R}$ could potentially be associated with higher accretion rates or larger black hole masses, as previous studies have found these quasar properties to correlate with L_{bol}. The remaining relationships are between $\mathcal{R}$ and the SFR, black hole mass, and λ_{Edd}. These (anti-)correlations are all found to be weak. Nevertheless, they can be closely related if a coevolution model of galaxies and SMBHs is considered (Cen (2012)). The coevolution model proposes three stages of galaxy evolution. These are the starburst period, the SMBH prime period and the Quiescent bulge period. The model is structured by SFR and SMBH accretion rate in accordance with the (anti-)correlations found here. Because of these connections, RL quasars are thought to be quasars in the earliest evolutionary stages, whereas RQ quasars are more evolved.

Having reviewed the results obtained in this thesis, it now remains to be discussed whether they could be improved for further research. As discussed in section 5.1, most errors are a result of a poor CIGALE modeling output. The inaccuracy of the modeling output is caused by both a faulty implemented dataset and a reduced amount of modeling parameters. Improving potential outcomes of the results must therefore start here. First of all, the dataset must be corrected for its faulty errors. As for the modeling by CIGALE, larger ranges of parameters are desired. For example, parameters used for the `sfhdelayed` module are currently kept at a minimum amount. Increasing the possible parameter values could increase the accuracy, as CIGALE has more parameters to model with. The following improvement is changing the dust emission module `dale2014` into `dl2014`. The `dl2014` module is based on a dust mixture of silicate grains, graphite grains, and PAHs. This module is more refined and more complex in comparison to `dale2014`, allowing for more parameters like the mass fraction of the PAHs (q_{PAH}

and the minimum radiation field ($U_{\min}$) to be evaluated. Another module of large importance yet unchanged for this project is the `radio` module. For starters, a smoother range of $frac_{\mathrm{AGN}}$ must be considered as to omit spikes in the finalized separated distribution. Additionally, the q_{IR} parameter must be updated to multiple values, to ensure accurate modeling of the dust emission as an effect of the FIRC. The final parameter of the `radio` module R_{AGN} needs updating as well, such that the SED represents a proper AGN fraction in the radio band which takes into account the contribution of SF. The updated parameters are listed in 5. Another factor to beneficially increase the results is to increase the quasar sample. To this end, more observational fields are necessary to be cross-matched. However, multiwavelength data is unfortunately not always available and a larger sample is therefore difficult to achieve.

The improvements mentioned above should be able to increase the accuracy of the results. An improvement of the results should provide a more refined $\mathcal{R}$ distribution, as the data needed for the SF removement tremendously improves. Further research into this field is therefore recommended. Because of the inaccurate modeling, the results obtained in this project are not extremely reliable. Nevertheless, the results do provide a guideline as to what is expected to be found from the methods described here. No apparent radio dichotomy quasar is found, even after separating the SF contribution from $\mathcal{R}$. Because of this indecisive result, the debate about the quasar radio dichotomy persists. Further research with improved methods and data is needed to provide further insight into the nature of RQ and RL quasars.

7 Acknowledgements

I would like to express my deepest gratitude to my supervisor Dr. Lingyu Wang for providing me with knowledge and feedback. I am also very grateful to Ph.D. student Antonio La Marca for his patience and help regarding the execution of the methods. Additionally, I would like to thank my fellow student Abel Kersten who inspired me and helped me continue where I was stuck.

References

Baloković, M. et al. (2012). Disclosing the Radio Loudness Distribution Dichotomy in Quasars: An Unbiased Monte Carlo Approach Applied to the SDSS-FIRST Quasar Sample. *The Astrophysical Journal*, 759(1).

Best, P. N. et al. (2005). The Host Galaxies of Radio-Loud Active Galactic Nuclei: Mass Dependences, Gas Cooling and Active Galactic Nuclei Feedback. *Monthly Notices of the Royal Astronomical Society*, 362(1):25–40.

Bian, W.-H. and Zhao, Y.-H. (2003). Accretion Rates and the Accretion Efficiency in AGNs. *Publications of the Astronomical Society of Japan*, 55(3):599–603.

Blandford, R. D. and Payne, D. G. (1982). Hydromagnetic Flows from Accretion Disks and the Production of Radio Jets. *Monthly Notices of the Royal Astronomical Society*, 199:883–903.

Blandford, R. D. and Znajek, R. L. (1997). Electromagnetic Extraction of Energy from Kerr Black Holes. *Monthly Notices of the Royal Astronomical Society*, 179(3):433–456.

Boquien, M. et al. (2019). CIGALE: a python Code Investigating GALaxy Emission. *Astronomy & Astrophysics*, 622.

Bruzual, G. and Charlot, S. (2003). Stellar Population Synthesis at the Resolution of 2003. *Monthly Notices of the Royal Astronomical Society*, 344(4):1000–1028.

Calzetti, D., Armus, L., Bohlin, R. C., Kinney, A. L., et al. (2000). The Dust Content and Opacity of Actively Star-forming Galaxies. *The Astrophysical Journal*, 553(2):682–695.

Cen, R. (2012). Physics of Coevolution of Galaxies and Supermassive Black Holes. *The Astrophysical Journal*, 755(28).

Cirasuolo, M., Magliocchetti, M., Celotti, A., and Danese, L. (2003). The Radio-loud/Radio-quiet Dichotomy: News from the 2dF QSO Redshift Survey. *The Astrophysical Journal*, 341(3).

Condon, J. J. (1992a). Radio Emission from Normal Galaxies. *Annual Review of Astronomy and Astrophysics*, 30:575–611.

Condon, J. J. (1992b). Radio Emission from Normal Galaxies. *Annual Review of Astronomy and Astrophysics*, 30:575–611.

Dale, D. A., Helou, G., Magdis, G. E., Armus, L., et al. (2014). A Two-parameter Model for the Infrared/Submillimeter/Radio Spectral Energy Distributions of Galaxies and Active Galactic Nuclei. *The Astrophysical Journal*, 784(1).

Dawson, K. S., Kneib, J.-P., Percival, W. J., Alam, S., et al. (2016). The SDSS-IV Extended Baryon Oscillation Spectroscopic Survey: Overview and Early Data. *The American Astronomical Society*, 151(2).

de Jong, T., Klein, U., Wielebinski, R., and Wunderlich, E. (1985). Radio Continuum and Far-infrared Emission from Spiral Galaxies: a Close Correlation. *Astronomy & Astrophysics*, 147:L6–L9.

Doi, A. et al. (2013). Very Long Baseline Array Imaging of Parsec-scale Radio Emissions in Nearby Radio-quiet Narrow-line Seyfert 1 Galaxies. *The Astrophysical Journal*, 765(1).

Dunlop, J. S. et al. (2003). Quasars, Their Host Galaxies and Their Central Black Holes. *Monthly Notices of the Royal Astronomical Society*, 340(4):1095–1135.

Fazio, G. G., Hora, J. L., Allen, L. E., Ashby, M. L. N., et al. (2004). The Infrared Array Camera (IRAC) for the Spitzer Space Telescope. *The Astrophysical Journal Supplement Series*, 154(1):10–17.

Ferrarese, L. and Merritt, D. (2000). A Fundamental Relation Between Supermassive Black Holes and Their Host Galaxies. *The Astrophysical Journal*, 539:L9–L12.

Garofalo, D. and Bishop, K. (2020). Evidence for Radio Loud to Radio Quiet Evolution from Red and Blue Quasars. *Publications of the Astronomical Society of the Pacific*, 132(1017).

Garofalo, D., North, M., Belga, L., and Waddell, K. (2020). Why Radio Quiet Quasars Are Preferred over Radio Loud Quasars Regardless of Environment and Redshift. *The Astrophysical Journal*, 890(2).

Gaur, H., Gu, M., Ramya, S., and Guo, H. (2019). Properties of Radio-loud Quasars in the Sloan Digital Sky Survey. *Astronomy & Astrophysics*, 631(A46):612–624.

Goldschmidt, P., Kukula, M. J., Miller, L., and Dunlop, J. S. (1999). A Comparison of the Optical Properties of Radio-loud and Radio-quiet Quasars. *The Astrophysical Journal*, 511:612–624.

Griffin, M. J. et al. (2010). The Herschel-SPIRE instrument and its in-flight performance* . *Astronomy & Astrophysics*, 518(L3).

Gürkan, G. et al. (2019). LoTSS/HETDEX: Optical quasars I. Low-frequency radio properties of Optically Selected Quasars. *Astronomy & Astrophysics*, 622(A11).

Hale, C. L., Williams, W., Jarvis, M. J., Hardcastle, M. J., et al. (2019). LOFAR Observations of the XMM-LSS Field. *Astronomy & Astrophysics*, 622(A4).

Hardcastle, M. J., Gürkan, G., van Weeren, R. J., Williams, W. L., et al. (2016). LOFAR/H-ATLAS: a deep low-frequency survey of the Herschel-ATLAS North Galactic Pole field. *Monthly Notices of the Royal Astronomical Society*, 462(2):1910–1936.

Helou, G., Soifer, B. T., and Rowan-Robinson, M. (1985). Thermal Infrared and Nonthermal Radio: Remarkable Correlation in Disks of Galaxies. *Astrophysical Journal*, 298:L7–L11.

Hill, G. J., Gebhardt, K., Komatsu, E., Drory, N., et al. (2008). The Hobby-Eberly Telescope Dark Energy Experiment (HETDEX): Description and Early Pilot Survey Results. *Panoramic Views of Galaxy Formation and Evolution ASP Conference Series*, 399.

Ho, L. C. (2002). On the Relationship between Radio Emission and Black Hole Mass in Galactic Nuclei. *The Astrophysical Journal*, 564(1):120–132.

Hurley, P. D., Oliver, S., Betancourt, M., Clarke, C., et al. (2017). HELP: XID+, the probabilistic de-blender for Herschel SPIRE maps. *Monthly Notices of the Royal Astronomical Society*, 464(1):885–896.

Inoue, A. K. (2011). Rest-frame Ultraviolet-to-optical Spectral Characteristics of Extremely Metal-poor and Metal-free Galaxies. *Monthly Notices of the Royal Astronomical Society*, 415(3):2920–2931.

Ivezić, Ž., Menou, K., Knapp, G. R., Strauss, M. A., Lupton, R. H., et al. (2002). Optical and Radio Properties of Extragalactic Sources Observed by the FIRST Survey and the Sloan Digital Sky Survey. *The Astronomical Journal*, 124(5):2364–2400.

Jiang, L. et al. (2007). The Radio-loud Fraction of Quasars is a Strong Function of Redshift and Optical Luminosity. *The Astrophysical Journal*, 656(2):680–690.

Kellermann, K. I. (1964). The Spectra of Non-Thermal Radio Sources. *The Astrophysical Journal*, 140.

Kellermann, K. I., Condon, J. J., Kimball, A. E., Perley, R. A., and Ž. Ivezić (2016). Radio-loud and Radio-quiet QSOs. *The Astrophysical Journal*, 831(2).

Kellermann, K. I., Sramek, R., Schmidt, M., Shaffer, D. B., and Green, R. (1989). VLA Observations of Objects in the Palomar Bright Quasar Survey. *Astronomical Journal*, 98.

Kenter, A., Murray, S. S., Forman, W. R., Jones, C., et al. (2005). XBootes: An X-Ray Survey of the NDWFS Bootes Field. II. The X-Ray Source Catalog. *The Astrophysical Journal Supplement Series*, 161(1).

Kondapally, R., Best, P. N., Hardcastle, M. J., Nisbet, D., et al. (2021). The LOFAR Two-meter Sky Survey: Deep Fields Data Release 1. III. Host-galaxy Identifications and Value Added Catalogues. *Astronomy & Astrophysics*, 648(A3).

Kormendy, J. and Richstone, D. (1995). Inward Bound—The Search for Supermassive Black Holes in Galactic Nuclei. *Annual Review of Astronomy and Astrophysics*, 33.

Körding, E. G., Jester, S., and Fender, R. (2007). Measuring the Accretion Rate and Kinetic Luminosity Functions of Supermassive Black Holes. *Monthly Notices of the Royal Astronomical Society*, 383(1):277–288.

Lacy, M. et al. (2001). The Radio Luminosity-Black Hole Mass Correlation for Quasars from the FIRST Bright Quasar Survey and a "Unification Scheme" for Radio-loud and Radio-quiet Quasars. *The Astrophysical journal*, 551(1).

Laor, A. (2000). On Black Hole Masses and Radio Loudness in Active Galactic Nuclei. *The American Astronomical Society*, 543(2).

Lyke, B. W. et al. (2020). The Sloan Digital Sky Survey Quasar Catalog: Sixteenth Data Release. *The Astrophysical Journal Supplement Series*, 250(1).

Macfarlane, C. et al. (2021). The Radio Loudness of SDSS Quasars from the LOFAR Two-metre Sky Survey: Ubiquitous Jet Activity and Constraints on Star Formation. *Monthly Notices of the Royal Astronomical Society*, 506(4):5888–5907.

Magorrian, J. et al. (1998). The Demography of Massive Dark Objects in Galaxy Centers. *The Astronomical Journal*, 115:2285–2305.

Mandal, S., Prandoni, I., Hardcastle, M. J., Shimwell, T. W., et al. (2021). Extremely Deep 150 MHz Source Counts from the LoTSS Deep Fields. *Astronomy & Astrophysics*, 648(A5).

McCheyne, I., Oliver, S., Sargent, M., Kondapally, R., et al. (2022). The LOFAR Two-metre Sky Survey Deep fields. *Astronomy & Astrophysics*, 662(A100).

Meiksin, A. (2006). Colour Corrections for High-redshift Objects due to Intergalactic Attenuation. *Monthly Notices of the Royal Astronomical Society*, 365(3):807–812.

Metcalf, R. B. and Magliocchetti, M. (2006). The Role of Black Hole Mass in Quasar Radio Activity. *Monthly Notices of the Royal Astronomical Society*, 365(1):101–109.

Murphy, E. J. (2009). The Far-Infrared-Radio Correlation at High Redshifts: Physical Considerations and Prospects for the Square Kilometer Array. *The Astrophysical Journal*, 706(1):482–496.

Murray, S. S., Austin, G. K., Chappell, J. H., Gomes, J. J., et al. (2000). In-flight Performance of the Chandra High-resolution Camera. *SPIE*, 4012:68–80.

Myers, A. D., Palanque-Delabrouille, N., Abhishek Prakash, I. P., Yeche, C., Dawson, K. S., Bovy, J., Lang, D., Schlegel, D. J., and Newman, J. A. (2015). The SDSS-IV Extended Baryon Oscillation Spectroscopic Survey: Quasar Target Selection. *The Astrophysical Journal Supplement Series*, 221(2).

Nagar, N. M., Falcke, H., and Wilson, A. S. (2005). Radio sources in Low-luminosity Active Galactic Nuclei. IV. Radio Luminosity Function, Importance of Jet Power, and Radio Properties of the Complete Palomar Sample. *Astronomy and Astrophysics*, 435(2):521–543.

Padovani, P. et al. (2017). Active Galactic Nuclei: What's in a Name? *The Astronomy and Astrophysics Review*, 25(2).

Panessa, F. et al. (2019). The Origin of Radio Emission from Radio-quiet Active Galactic Nuclei. *Nature Astronomy*, 3:387–396.

Pilbratt, G. L. et al. (2010). Herschel Space Observatory. An ESA facility for far-infrared and submillimetre astronomy. *Astronomy & Astrophysics*, 518(L1).

Poglitsch, A., Waelkens, C., Geis, N., Feuchtgruber, H., et al. (2010). The Photodetector Array Camera and Spectrometer (PACS) on the Herschel Space Observatory*. *Astronomy & Astrophysics*, 518(L2).

Predehl, P., Böhringer, H., Brunner, H., Brusa, M., et al. (2021). eROSITA on SRG. *Astronomy & Astrophysics*, 647(A1).

Radcliffe, J. F. (2021). The radio emission from active galactic nuclei. *Astronomy & Astrophysics*, 649(L9).

Retana-Montenegro, E. and Röttgering, H. J. A. (2017). Probing the Radio Loud/Quiet AGN Dichotomy with Quasar Clustering. *Astronomy & Astrophysics*, 600(A97).

Richards, G. T. et al. (2006). The Sloan Digital Sky Survey Quasar Survey: Quasar Luminosity Function from Data Release 3. *The Astronomical Journal*, 131(6):2766–2787.

Rieke, G. H., Young, E. T., Engelbracht, C. W., Kelly, D. M., et al. (2004). The Multiband Imaging Photometer for Spitzer (MIPS). *The Astrophysical Journal Supplement Series*, 154(1):25–29.

Sabater, J., Best, P. N., Tasse, C., Hardcastle, M. J., et al. (2021). The LOFAR Two-meter Sky Survey: Deep Fields Data Release 1. II. The ELAIS-N1 LOFAR deep field. *Astronomy & Astrophysics*, 648(A2).

Shimwell, T. W., Hardcastle, M. J., Tasse, C., Best, P. N., et al. (2022). The LOFAR Two-metre Sky Survey. *Astronomy & Astrophysics*, 659(A1).

Sikora, M., Ł. Stawarz, and Lasota, J.-P. (2007). Radio Loudness of Active Galactic Nuclei: Observational Facts and Theoretical Implications. *The Astrophysical Journal*, 658(2):815–828.

Stalevski, M., Fritz, J., Baes, M., Nakos, T., and Popović, L. Č (2012). 3D Radiative Transfer Modelling of the Dusty Tori around Active Galactic Nuclei as a Clumpy Two-phase Medium. *Monthly Notices of the Royal Astronomical Society*, 420(4):2756–2772.

Stalevski, M., Ricci, C., Ueda, Y., Lira, P., et al. (2016). The Dust Covering Factor in Active Galactic Nuclei. *Monthly Notices of the Royal Astronomical Society*, 458(3):2288–2302.

Stocke, J. T., Morris, S. L., Weymann, R. J., and Foltz, C. B. (1992). The Radio Properties of the Broad-Absorption-Line QSOs. *The Astrophysical Journal*, 396.

Strittmatter, P. A. et al. (1980). Radio Observations of Optically Selected Quasars. *Astronomy & Astrophysics*, 88(3):L12–L15.

Tasse, C., Shimwell, T., Hardcastle, M. J., P., S. O., et al. (2021). The LOFAR Two-meter Sky Survey: Deep Fields Data Release 1. I. Direction-dependent calibration and imaging. *Astronomy & Astrophysics*, 648(A1).

van der Kruit, P. C. (2005). Observations of Core Sources in Seyfert and Normal Galaxies with the Westerbork Synthesis Radio Telescope at 1415 MHz. *Astronomy & Astrophysics*, 15:110 – 122.

White, R. L. et al. (2007). Signals from the Noise: Image Stacking for Quasars in the FIRST Survey. *The Astrophysical Journal*, 654(1):99–114.

Wright, E. L., Eisenhardt, P. R. M., Mainzer, A. K., Ressler, M. E., et al. (2010). The Wide-field Infrared Survey Explorer (WISE): Mission Description and Initial On-orbit Performance. *The Astronomical Journal*, 140(6):1868–1881.

Wu, Q. and Shen, Y. (2022). A Catalog of Quasar Properties from Sloan Digital Sky Survey Data Release 16. *The Astrophysical Journal Supplement Series*, 263(2):42.

Xie, G. Z., Zhou, S. B., and Liang, E. W. (2004). The Mass-Luminosity Relation, Accretion Rate-Luminosity Relation, and Evolutionary Sequence of Blazars. *The American Astronomical Society*, 127(1).

Yang, G., Boquien, M., Buat, V., and Burgarella, D. (2020). X-CIGALE: Fitting AGN/galaxy SEDs from X-ray to infrared. *Monthly Notices of the Royal Astronomical Society*, 491(1):740–757.

Yang, G. et al. (2022). Fitting AGN/Galaxy X-Ray-to-radio SEDs with CIGALE and Improvement of the Code. *The Astrophysical Journal*, 927(2).

Yun, M. S., Reddy, N. A., and Condon, J. J. (2001). Radio Properties of Infrared-selected Galaxies in the IRAS 2 Jy Sample. *The Astrophysical Journal*, 554(2):803–822.

Zakamska, N. L. et al. (2016). Star Formation in Quasar Hosts and the Origin of Radio Emission in Radio-quiet Quasars. *Monthly Notices of the Royal Astronomical Society*, 455(4).

8 Appendix

Parameter	Value	Description
Star Formation History		
τ_{main}	100, 500, 1000, 5000	E-folding time of the main stellar population model in Myr.
Age	500, 1000, 3000, 5000, 7000	Age of the main stellar population in the galaxy in Myr.
Stellar Emission		
imf	Chabrier (2003)	Initial Mass Function
Dust Attenuation		
$E_{BV_{lines}}$	0, 0.02, 0.05, 0.1, 0.2, 0.4, 0.7, 0.9	E(B - V) lines, the color excess of the nebular lines light for both the young and old population.
AGN Emission		
i	30, 70	inclination, i.e. viewing angle, position of the instrument w.r.t. the AGN axis.
δ	-1, -0.8, -0.6, -0.4, -0.2, -0.1, 0, 0.1, 0.2, 0.4, 0.6, 0.8, 1	Power-law of index δ modifying the optical slope of the disk.
$frac_{AGN}$	0, 0.1, 0.2, 0.4, 0.6, 0.8, 0.99	AGN fraction.
$\lambda_{frac_{AGN}}$	0.685/0.84	Wavelength range in microns where to compute the AGN fraction.
EBV	0, 0.01, 0.05, 0.1, 0.4, 0.7, 1	E(B-V) for the extinction in the polar direction in magnitudes.
X-ray Emission		
α_{ox}	-1.9	Power-law slope connecting L_ν at rest-frame 2500 AA and 2 keV.
$max_{\alpha_{ox}}$	10	Maximum allowed deviation of α_{ox} from the empirical $\alpha_{ox} - L_\nu$(2500 AA) relation (Just et al. 2007)

Table 4: Parameters chosen for the CIGALE configuration file, used in the SED fitting. Only parameters with values that differ from the default ones are shown.

Parameter	Value	Description
Star Formation History		
τ_{main}	500, 1000, 2000, 4000, 6000, 8000	E-folding time of the main stellar population model in Myr.
Age	500, 1000, 2000, 3000, 4000, 5000, 8000	Age of the main stellar population in the galaxy in Myr.
τ_{burst}	500, 9000, 13000	E-folding time of the late starburst population model in Myr.
Burst Age	10, 30, 100, 300	Age of the late burst in Myr.
f_{burst}	0.00, 0.10, 0.20, 0.30	Mass fraction of the late burst population.
Stellar Emission		
imf	Chabrier (2003)	Initial Mass Function
Dust Attenuation		
$E_{BV_{lines}}$	0, 0.05, 0.1, 0.2, 0.4, 0.5, 0.8	E(B - V) lines, the color excess of the nebular lines light for both the young and old population.
$E_{BV_{factor}}$	1	The stellar continuum attenuation. Both young and old population are attenuated.
Dust Emission		
q_{PAH}	0.47, 1.12, 2.50, 3.9, 4.58, 5.95	Mass fraction of PAH.
U_{min}	0.5, 1.00, 5.00, 10.00, 20.00	Minimum radiation field.
α	1.7, 2.0, 2.3	Powerlaw slope dU/dM $\propto U^{\alpha}$.
γ	0.02	Fraction illuminated from U_{min} to U_{max}.
AGN Emission		
i	30, 70	inclination, i.e. viewing angle, position of the instrument w.r.t. the AGN axis.
δ	-1, -0.8, -0.6, -0.4, -0.2, 0, 0.2, 0.4, 0.6, 0.8, 1	Power-law of index δ modifying the optical slope of the disk.
$frac_{AGN}$	0, 0.1, 0.2, 0.3, 0.4, 0.5, 0.6, 0.7, 0.8, 0.9, 0.99	AGN fraction.
$\lambda_{frac_{AGN}}$	0.685/0.84	Wavelength range in microns where to compute the AGN fraction.
EBV	0, 0.2, 0.4, 0.7	E(B-V) for the extinction in the polar direction in magnitudes.
X-ray Emission		
α_{ox}	-1.9	Power-law slope connecting L_{ν} at rest-frame 2500 \AA and 2 keV.
$max_{\alpha_{ox}}$	10	Maximum allowed deviation of α_{ox} from the empirical $\alpha_{ox} - L_{\nu}(2500\text{Å})$ relation (Just et al. 2007)
Radio Emission		
q_{IR}	2.4, 2.5, 2.6, 2.7	The value of the FIR/radio correlation coefficient for star formation.
α_{SF}	0.8	The slope of the power-law synchrotron emission related to star formation, $L_{\nu} \propto \nu^{-\alpha}$.
R_{AGN}	0, 0.01, 0.1, 1, 10, 100, 1000, 5000	The radio-loudness parameter for AGN, defined as $R = L_{\nu}(5\text{GHz})/L_{\nu}(2500\text{Å})$, where $L_{\nu}(2500\text{Å})$ is the AGN 2500 Å intrinsic disk luminosity measured at viewing angle = 30°.

Table 5: Proposal for refined parameter input for the CIGALE configuration file, used in the SED fitting. Only parameters with values that differ from the default ones are shown.

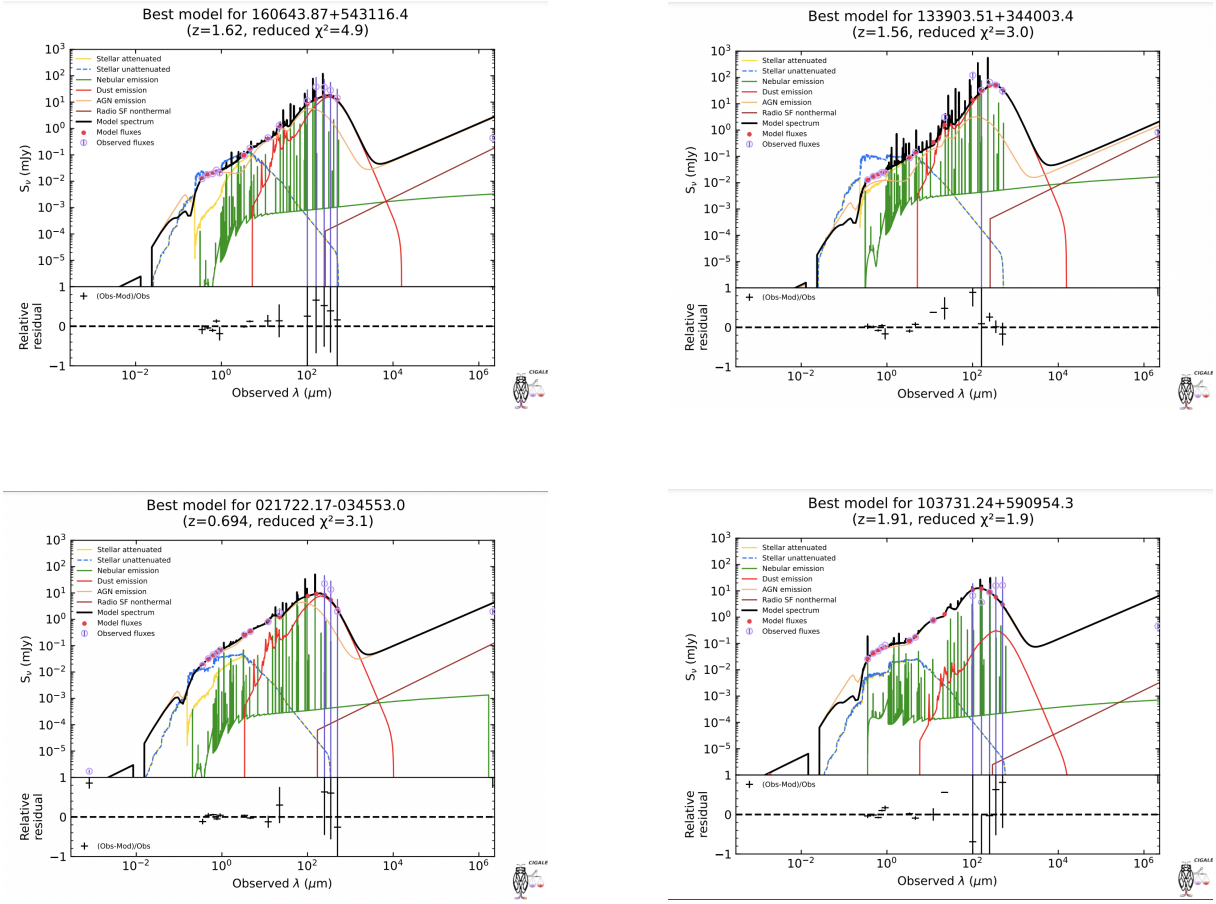

Figure 20: Four randomly selected "good" best-fitted SEDs that were created using CIGALE. Parameters used for this result are given in Table 4. The reason these models were used for the data analysis is because $\chi^2 < 5$ and dust emission is present.

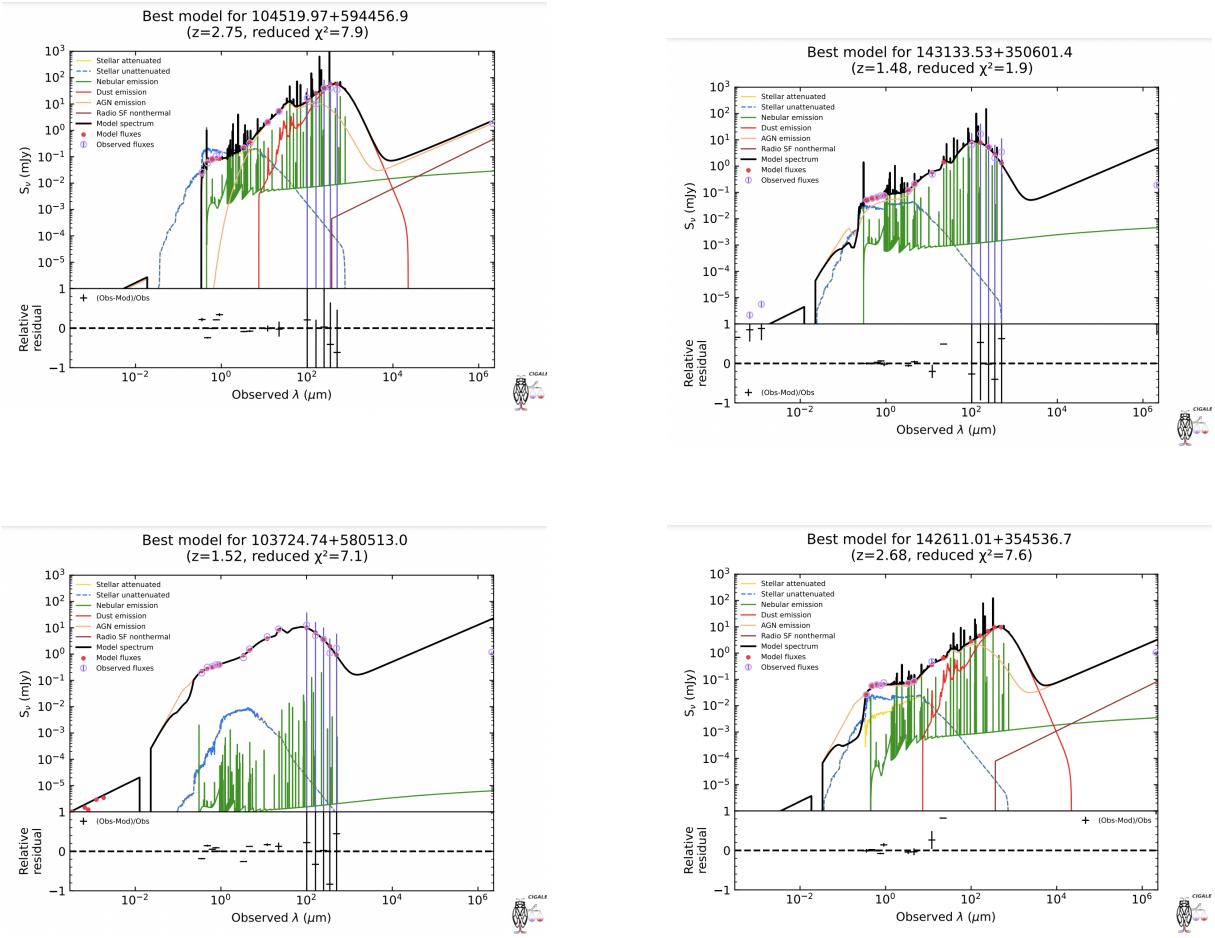

Figure 21: Four randomly selected "bad" best-fitted SEDs that were created using CIGALE. Parameters used for this result are given in Table 4. Data from these SEDs are not used for data analysis for the following reasons. Either $\chi^2 > 5$ or no dust emission is present. Some SEDs have a combination of both.

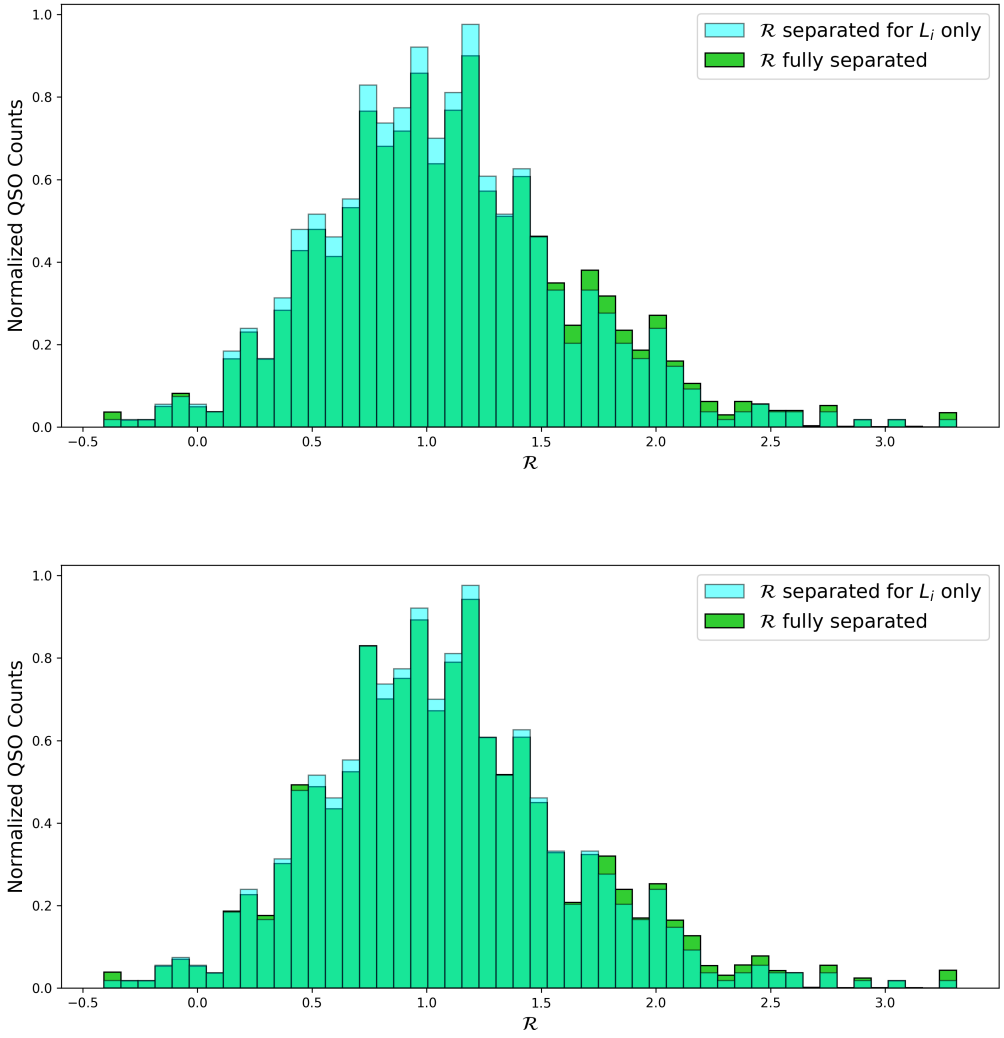

Figure 22: Presented are two histogram comparisons. In both graphs the $\mathcal{R}$ distribution where the SF component is removed for both L_{144} and L_i is compared to the $\mathcal{R}$ distribution where that is only true for L_i. The different results are due to the random gaussian sampling method (see section 3.3). The fully separated $\mathcal{R}$ distribution used for data-analysis is not given here. This distribution is shown in figure 13. Similar to this figure, the fully separated $\mathcal{R}$ distribution appears to be more radio-loud.